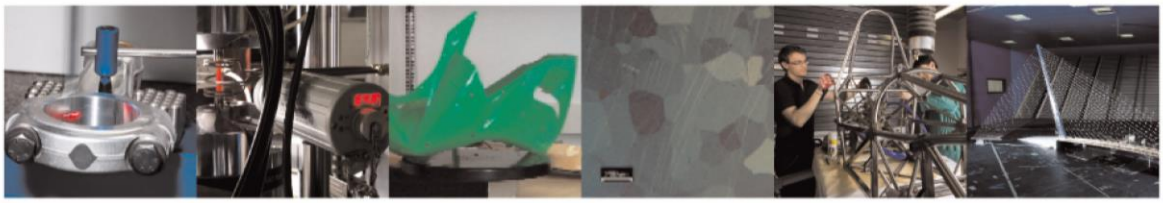

Novel Zn-based alloys for biodegradable stent applications: Design, development and in vitro degradation

Mostaed, E.; Sikora-Jasinska, M.; Mostaed, A.; Loffredo, S.; Demir, A.G.; Previtali, B.; Mantovani, D.; Beanland, R.; Vedani, M.

This is a post-peer-review, pre-copyedit version of an article published in JOURNAL OF THE MECHANICAL BEHAVIOR OF BIOMEDICAL MATERIALS. The final authenticated version is available online at: http://dx.doi.org/10.1016/j.jmbbm.2016.03.018

Novel Zn-based alloys for biodegradable stent applications: Design, Development and In Vitro Degradation

E. Mostaed[a,1], M. Sikora-Jasinska[a,b], A. Mostaed[c], S. Loffredo[a], A. G. Demir[a], B. Previtali[a], D. Mantovani[b], R. Beanland[c], M. Vedani[a]

[a] Department of Mechanical Engineering, Politecnico di Milano, Milan, Italy.

[b] Lab. for Biomaterials & Bioengineering (CRC-I), Dept. Min-Met-Materials Engineering & Research Center CHU de Québec, Laval University, Québec City, Canada.

[c]Department of Physics, University of Warwick, Coventry, UK.

Abstract

The search for a degradable metal simultaneously showing mechanical properties equal or higher to that of stainless steel and uniform degradation is still an open challenge. Several magnesium-based alloys have been studied, but their degradation rate has proved to be too fast and rarely homogenous. Fe-based alloys show appropriate mechanical properties but very low degradation rate. In the present work, four novel Zn-Mg and two Zn-Al binary alloys were investigated as potential biodegradable materials for stent applications. The alloys were developed by casting process and homogenized at 350 °C for 48 hours followed by hot extrusion at 250 °C. Tube extrusion was performed at 300°C to produce tubes with outer/inner diameter of 4/1.5 mm as precursors for biodegradable stents. Corrosion tests were performed using Hanks' modified solution. Extruded alloys exhibited slightly superior corrosion resistance and slower degradation rate than those of their cast counterparts, but all had corrosion rates roughly half that of a standard purity Mg control. Hot extrusion of Zn-Mg alloys shifted the corrosion regime from localized pitting to more uniform erosion, mainly due to the refinement of second phase particles. Zn-0.5Mg is the most promising material for stent applications with a good combination of strength, ductility, strain hardening exponent and an appropriate rate of loss of mechanical integrity during degradation. An EBSD analysis in the vicinity of the laser cut Zn-0.5Mg tube found no grain coarsening or texture modification confirming that, after laser cutting, the grain size and texture orientation of the final stent remains unchanged. This work shows the potential for Zn alloys to be considered for stent applications.

Keywords: Zn alloys, Biodegradable stent, Extrusion, Mechanical properties, Texture, Corrosion behavior, Laser cutting.

[1] **Corresponding Author:**
Ehsan Mostaed
Department of Mechanical Engineering, Politecnico di Milano, Via La Masa 1, 20156 Milan, Italy
Email: ehsan.mostaed@polimi.it
Tel: +39 02 23998661
Fax: +39 02 23998644

1. Introduction

Biodegradable metallic materials have received much attention as ideal temporary implants due to their combination of mechanical properties and biocompatibility. In the last decade iron and magnesium, both pure and alloyed, have been extensively studied as potential materials for bioabsorbable cardiovascular stents (Al-Abdullat et al., 2001; Erbel et al., 2007; Hermawan et al., 2010; Li et al., 2004, 2008; Peuster et al., 2001; Witte et al., 2005). However, Mg and most of its alloys corrode too rapidly in physiological environments, reducing the stent mechanical integrity during the arterial vessel remodeling which is complete within 6 to 12 months (Di Mario et al., 2004; Mm et al., 2001). While the corrosion rate of high purity Mg is thousands of times less than standard purity Mg one in Hank's solution (Song, 2007), its poor mechanical properties restrict it from cardiovascular application. The mechanical properties of Mg can be improved by introducing alloying elements, or grain refinement through precipitate and grain boundary strengthening (Gu et al., 2009; Ehsan Mostaed et al., 2015a, 2015b; Mostaed et al., 2013; Ogushi et al., 2014; Wang et al., 2016; Witte et al., 2008). Grain refinement of Mg alloys to an ultra-fine regime leads to a more uniform corrosion mode, mainly as a result of secondary phase refinement and redistribution (Mostaed et al., 2014a; Qiang et al., 2014; Zeng et al., 2011). Among all Mg alloys, WE43 appears to be one of the most promising candidates due to its good mechanical properties and low corrosion rate (Gu et al., 2010). However, WE43 coronary stents have been found to lose mechanical integrity in less than 4 weeks whereas the desirable service time is at least 6 months (Di Mario et al., 2004; Onuma et al., 2011).

In contrast, while Fe exhibits superior mechanical properties compared to Mg, in vivo animal tests have shown a very slow degradation rate. A typical study (Peuster et al., 2006) showed that large portions of a pure Fe stent remained intact in the blood vessels even twelve months post-surgery. Furthermore, Pierson et al. (Pierson et al., 2012) demonstrated that corrosion products of iron are stable in physiological environments, resulting in long-term retention that challenge the long-term integrity of the artery.

Therefore, despite many attempts to improve Mg and Fe implant properties, attention is now being focused on alternative materials such as Zn (Bowen et al., 2013; Gong et al., 2015; Murni et al., 2015; Vojtěch et al., 2011). Zinc has a standard corrosion potential of -0.8V, intermediate between Fe (-0.4V) and Mg (-2.4V) (Cheng et al., 2013). Furthermore, Zn is an essential element in human nutrition and is the second most abundant transition metal element in the human body, playing a crucial role in cell proliferation as well as the immune and nervous

systems (Lastra et al., 2001; Saltman and Strause, 1993). It also serves as a cofactor for catalytic function of enzymes (McCall et al., 2000). The recommended daily intake value of Zn starts from 2-3 mg day $^{-1}$ for infants up to 8-11 mg day $^{-1}$ for adults. It is reported that, excess Zn in the body is harmful to vital organs such as the kidney, spleen, liver, brain and heart. Moreover, long-term exposure or high-dose Zn interferes with the uptake of copper (Plum et al., 2010; TRUMBO et al., 2001). However, in case of cardiovascular stent application, considering the cut stent weight of about 50 mg and complete degradation between 6 to 12 months, the daily dose of Zn is significantly below the recommended daily values for adults and infants (Bowen et al., 2013; Xu et al., 2007). Bowen et al. (Bowen et al., 2015, 2013) have reported the only in vivo studies to date, implanting pure Zn wire into rat abdominal aorta for up to 6 months. It was proved that Zn could remain intact for 4 months and afterward the corrosion accelerated, indicating timely degradation of the implant. It was also shown that after 4.5 and 6 months in vivo, the corrosion products were primarily benign compacted zinc oxide interspersed in zinc carbonate (Bowen et al., 2013). They also showed that after partial degradation, tissue regenerated within the original footprint of the implant. More importantly, they proved that Zn has an antiproliferative effect, guarding against restenosis after stent implantation (Bowen et al., 2015).

Alongside its biocompatibility and being an essential element in the human body, Zn has a low melting point (420 °C) and low reactivity in the molten state (unlike Mg), permitting melting and hot processing in air. Nevertheless, the tensile strength of as-cast pure Zn is < 20 MPa (Vojtěch et al., 2011), far too low for cardiovascular stents. Improvements in mechanical properties can be produced by adding alloying elements and/or thermomechanical refinement of grain size by extrusion, rolling, forging etc. (Li et al., 2015; L. Liu et al., 2015; E. Mostaed et al., 2015; Mostaed et al., 2014b; Pan et al., 2015; Park et al., 2015; Tong et al., 2015; Wang et al., 2016). However, any alloying elements must be carefully selected to have only benign effects on biocompatibility. For example, it is known that Al-containing Mg alloys are potentially toxic since aluminum ions can combine with inorganic phosphates, causing a lack of phosphate in the human body (Witte et al., 2008). Unfortunately, many widely-used Zn-based alloys contain large amounts of Al (e.g. ZA8, ZA12 and ZA27 with 8–27 wt.% Al, 1–3 wt.% Cu) and are therefore unsuitable for bioapplications (Babic et al., 2010; Pandey et al., 1998; Pürçek et al., 2002; Savaskan and Murphy, 1987). New biodegradable Zn-based alloys, containing limited amounts of Al or other potentially harmful elements, are therefore of interest. Mg, as a well-studied biocompatible metal, is an obvious choice of alloying element. Zn-Mg binary alloys may be expected to have superior mechanical properties while maintaining high biosafety. There are as yet few studies of Zn-Mg

alloys as new bioabsorbable implant materials and their microstructural and mechanical properties. Vojtech et al. (Vojtěch et al., 2011) investigated mechanical and corrosion behavior of as-cast Zn-Mg binary alloys with different Mg contents (from 1 to 3wt.%). They found that adding 1wt.% Mg improved mechanical strength considerably, from 20 to about 190 MPa through the formation of a $Zn+Mg_2Zn_{11}$ eutectic mixture, but they also recorded elongation-to-failure values below 2%. These properties would not be sufficient for many load-bearing applications in biodegradable devices since these typically require strengths >300 MPa and elongation-to-failure >15% (Bowen et al., 2013; Mani et al., 2007). Higher Mg contents would be expected to have an increased volume fraction of the brittle eutectic, giving even poorer ductility and fracture toughness. Hence, for demanding applications (e.g. stents) other methods to improve Zn-Mg alloy properties must be developed. Any material must also satisfy requirements for dissolution; corrosion evaluation has demonstrated that all Zn-Mg alloys show corrosion rates significantly lower than Mg regardless of Mg content. Additionally, processing minitubes for stents is not trivial; the material must have a good response to laser irradiation during strut cutting, and most importantly, microstructural stability study after laser cutting. Despite their importance, these factors are rarely reported in studies focusing on biodegradable metals development.

Here, pure Zn and several Zn-Mg alloys with Mg contents ranging from 0.15 to 3 wt.% are studied in detail. Their microstructural, mechanical and corrosion properties, as well as the feasibility of mini-tube processing, are systematically investigated. Furthermore, low Al-content Zn-Al alloys, containing 0.5 and 1wt.% Al are prepared and characterized. The potential of these alloys for stents is assessed by processing minitubes via warm extrusion. Subsequent laser cutting is used to investigate microstructural modifications that could impact the mechanical properties of the final product.

2. Experimental procedures

2.1. Materials and processing

Both binary Zn-Mg and Zn-Al alloys were investigated. Zn (99.995%), Mg (99.95%) and Al (99.995%) were melted at 500 °C in cylindrical steel molds inside a resistance furnace, producing cast cylindrical billets with a length and diameter of 80 mm and 15 mm, respectively. Table1 lists the compositions of all the produced alloys. Annealing at 350 ºC was conducted for 48 hours in order to homogenize the cast structure followed by water quenching. Annealed samples were subsequently extruded at 250°C with an extrusion ratio of 6:1 to obtain cylindrical rods. To prepare small tubes as a stent precursor, hot tube extrusion was conducted at 300°C

with an extrusion ratio of 16:1, giving a tube with outer and inner diameters of 4 and 1.5mm respectively. The extrusion die was heated by an induction heating system and the temperature was measured using a thermocouple inserted into the die through a drilled borehole. Before the extrusion, samples were put in the die, held for 10 min and then processed.

2.2. Microstructural characterization

All the investigated samples were cut by a diamond-blade saw to obtain longitudinal (i.e. parallel to the extrusion direction) sections. The samples were ground and polished following standard metallographic procedures and etched in a solution of 6g picric acid, 5 ml acetic acid, 10 ml water and 100 ml ethanol. Microstructure was observed by optical microscopy (OM) and field emission gun scanning electron microscopy (FEG-SEM). The evolution of the structure in extruded samples was assessed primarily by examination of longitudinal sections. Characterization of extruded tubes used interrupted extrusion, i.e. taking samples extracted from the die. These samples contained an undeformed billet region (thermally affected due to holding at high temperature), a transition zone (undergoing deformation) and the formed tube (combined effects of high temperature and plastic deformation), giving a wealth of information in sections containing the pressing direction (prepared by standard mechanical polishing followed by low-angle Ar^+ ion milling). Grain size distributions, crystallographic texture and grain orientation maps were obtained using Electron Backscattered Diffraction (EBSD) in a Zeiss Supra FEG-SEM. The data were processed with TSL OIM™ software.

2.3. Mechanical characterization

Mechanical properties after extrusion were evaluated by tensile, compression and Vickers micro-hardness tests. Following ASTM E8-04 specification (ASTM E8-04, 2004), dog-bone type tensile specimens with long axis along the extrusion direction were machined from extruded billets with a gage length of 12 mm, diameter of 4 mm and radius of fillet of 4 mm. Compression tests were carried out in accordance to ASTM E9-09 standard (ASTM E9-09, 2009) on cylindrical specimens with a diameter of 4 mm and height of 8 mm. Both tensile and compression tests were performed at room temperature and at an initial strain rate of 1×10^{-3} s^{-1}. In both tensile and compression tests, standard deviations were calculated in each case out of a population of three experiments. Micro-hardness measurements were made on a plane containing the extrusion direction with an indenter load of 5 N. The hardness value is the average of five different measurements. Due to their small size,

the mechanical properties of extruded tubes were characterized only by Vickers micro-hardness test. Vickers micro-hardness tests were also performed on the interrupted extrusion samples (the same samples used for microstructural characterization) allowing billet, transition and tube regions to be tested. In addition, the mechanical integrity of partially degraded materials was assessed by performing compression tests on the samples after 336 hours of immersion in Hanks' modified solution.

2.4. Corrosion behavior

The degradation behavior of Zn and Zn binary alloys was studied in Hanks' modified solution which simulates the ionic composition of blood plasma. The solution was prepared by dissolving Hanks' balanced salts (H1387) in 1.4 L of nanopure water with the addition of 14.16 g of HEPPES acid, (H3375-5000G, Sigma Aldrich, USA), 16.65 g of HEPPES sodium salt (H7006-500G, Sigma-Aldrich, USA) and 3.3 g of sodium bicarbonate (S8875-500G, Sigma-Aldrich, USA) as reported by Lévesque et al. (Lévesque et al., 2008). Both potentiodynamic polarization (ASTM G59–97) (ASTM G59-97 Standard Test Method for Conducting Potentiodynamic Polarization Resistance Measurements, 2003) and static immersion (ASTM G31-72) (2004, n.d.) tests were performed to investigate the corrosion resistance.

2.4.1. Potentiodynamic corrosion test

Electrochemical measurements were carried out with a traditional three-electrode cell using a Princeton Applied Research Model 273 galvanostat/potentiostat. Corrosion tests were accomplished at the scanning rate of 0.166 mV s^{-1} and applied potential from −1.5 to −0.2 V since the corrosion potential of zinc was predicted to be in this range based on previous studies (X. Liu et al., 2015; Törne et al., 2015). The specimen, a saturated calomel electrode (SCE) and a platinum electrode were used as the working electrode, reference electrode, and the auxiliary electrode, respectively. The samples were polished with 4000 grit SiC paper and 0.05μm alumina paste prior to electrochemical testing. The solution temperature and pH were adjusted to 37±1℃ and 7.4 respectively. The corrosion rate was calculated from the corrosion current density (i_{corr}) using:

$$CR = 3.27 \cdot 10^{-3} \frac{i_{corr} EW}{\rho} \quad (1)$$

where CR is the corrosion rate (mm·$year^{-1}$), i_{corr} is the corrosion current density (μA·cm^{-2}), EW is the equivalent weight of metal (i.e. 32.6 for pure Zn) and ρ is the density (g·cm^{-3}). For each type of material 4 specimens were tested and the mean value and standard deviation were calculated.

2.4.2. Static immersion test

The specimens were polished with 4000 grit SiC paper and 0.05 μm alumina paste before washing with ethanol for 5 min in ultrasonic bath to remove surface particles, and then rinsed with distilled water for 10 min. The Zn and Zn-based extruded alloy samples were weighed after drying and immersed for 336 hours in Hanks' modified solution under controlled conditions (T = 37±1℃, pH = 7.4). Approximately 70 ml Hanks' modified solution per cm^2 sample surface was used. The whole volume of solution was changed every 48 hours to keep the pH value close to 7.4 and to achieve conditions as constant as possible. Subsequently the samples were washed with 200 g L^{-1} of chromium oxide in order to remove corrosion products before measuring the final weight. The corrosion rates of the alloys were then calculated using the weight loss method:

$$CR = 8.74 \cdot 10^4 \frac{W}{A \cdot t \cdot \rho} \quad (2)$$

where CR is the corrosion rate ($mm \cdot year^{-1}$), W is weight loss (g), A is area (cm^2), t is time of exposure (h) and ρ is material density ($g \cdot cm^{-3}$). Four specimens were tested for each condition and the average value and standard deviation were calculated.

The surface morphologies and chemical compositions of the alloys both before and after corrosion testing were examined by scanning electron microscopy (SEM) and energy dispersion spectrometry (EDS).

2.5. Laser cutting

Laser microcutting was performed with a ns-pulsed fiber laser operating at 1064 nm (YLP 1/100/50/50 from IPG Photonics, Cambridge, MA, USA). The laser was coupled to a cutting head with coaxial nozzle for process gas supply (Micro from HighYAG, Kleinmachnow, Germany). Manipulation of Zn alloy micro tubes was achieved via a linear and a rotational axis (ALS-130 and ACS-150 from Aerotech, Pittsburgh, PA, USA). In this configuration the beam diameter at focal position is 19 μm. The cuts were realized using 11 W average power, 35 kHz pulse repetition rate, 2 mm/s linear velocity and Ar as the processing gas at 7 bar.

3. Results and discussions

3.1. Microstructural characterization

Fig.1 shows optical micrographs of the as-cast samples. It can be seen that as-cast pure Zn has very coarse grains (> 1mm), while alloying with Mg and Al produces a significantly refined structure. According to the Zn–

Mg equilibrium phase diagram (Butts and Gale, 2004), the microstructure of Mg-containing alloys consists of primary α-Zn dendritic grains in a matrix of Zn + Mg_2Zn_{11} eutectic (Fig. 1b to d). The larger Mg content leads to an increase in the volume fraction of the eutectic mixture and a decrease in the grain size of the alloys (see insets bottom right). Eventually, a fully eutectic structure with a fine lamellar structure of Zn and Mg_2Zn_{11} (Fig.1e) is obtained in the Zn-3Mg alloy.

The optical micrograph of Zn-0.5Al (Fig. 1f) shows a structure mainly composed of α-Zn solid solution due to the high solubility of Al in Zn (~1.1wt.% at 382 °C). Inspection at higher magnification revealed a small amount of eutectoid at grain boundaries (inset in Fig. 1f). Fig. 1g shows that the eutectoid mixture is more evident at grain boundaries in the Zn-1Al alloy due to the higher Al content. The presence of eutectoid may retard grain growth by pinning the grain boundaries thereby leading to a significantly finer microstructure.

Fig. 2 shows the microstructural evolution of Zn-1Al alloy during solution treatment (ST) at 24 hours (Fig. 2a and c) and 48 hours (Fig. 2b and d) at 350°C. After 24 hours the volume fraction of the eutectic decreases; it no longer forms a continuous grain boundary network and is fragmented into discontinuous colonies with lamellar morphology. After 48 hours, the eutectic constituent is further dissolved into the α-Zn matrix and the precipitates have a block-shaped morphology. Limited residual precipitates survive at grain boundaries (Fig. 2b and d and their corresponding EDS spectra), which suggests a condition close to saturation of Al in α-Zn solid solution. Accordingly, solution thermal treatment for all the samples was set at 350 ºC for 48 hours.

Fig. 3 shows the ST samples of the Zn-Mg alloys, with a microstructure preserved by the final rapid cooling. For alloys with a Mg concentration below the solid solubility limit (Fig. 3a and e) the eutectic and eutectoid structures seen in the as-cast material have dissolved, forming a supersaturated Zn solid solution. For alloys with Mg concentrations exceeding the solid solubility limit, the eutectic phase mixture in the interdendritic region has altered from a lamellar morphology to discrete Mg_2Zn_{11} particles at grain boundaries (see Fig. 3b, c and d).

EBSD maps, grain size distributions and (0001) pole figures of the extruded samples are shown in Fig.4. As seen in Fig. 4a, extruded pure Zn exhibits smaller grains (mean grain size of about 151 ± 19.6 μm) compared to its ingot counterpart, although the reduction in grain size is limited by extrusion at 250°C. Such a coarse microstructure obtained even after extrusion is consistent with the very low recrystallization temperature of pure Zn (close to room temperature (Freeman, 1926)), leading to fast grain growth after the extrusion process.

The extruded Zn-0.15Mg sample has a markedly smaller grain size (Fig. 4b) when compared to its solution treated counterpart (Fig. 3a). Indeed, the nearly equiaxed grains with a mean size of 6.6 ± 0.8 μm is consistent with dynamic recrystallization (DRX) during the extrusion. The introduction of Mg may induce particle stimulated nucleation (PSN), in which high-stress zones are formed around the hard Mg_2Zn_{11} phase, accelerating the DRX process and promoting the grain refinement effect (Robson et al., 2009). For the alloys containing 0.5 wt.% and 1 wt.% Mg, extrusion induced a change in microstructure from dendritic to equiaxed, with an average grain size of 4.1 ± 0.4 and 4.4 ± 0.5 μm, respectively. SEM images of the extruded Zn-Mg samples are shown in Fig. 5. As seen, with increasing Mg content, the volume fraction of the dark particles consistently increases ending up with reasonably homogeneous distribution of these particles throughout the microstructure in Zn-3Mg alloy. An EDS analysis on Zn-0.5Mg sample shows that the matrix is α-Zn with a small amount of Mg, while the dark grains are the Mg-Zn intermetallic phase (Fig. 5b). Therefore, it can be supposed that the network-like Mg_2Zn_{11} phase in the solution-treated samples is changed by the warm extrusion process into Mg_2Zn_{11} precipitates, arranged along the extrusion direction. Moreover, the grain size apparently reaches a saturation level since addition of 0.5 wt.% Mg and even higher amounts have only minor effects on grain size (Fig. 4c,d).

In case of Al bearing alloys, an equiaxial grain structure is found in longitudinal cross-sections (Fig.4e, f), confirming the occurrence of considerable grain refinement after extrusion. However, unlike Mg containing alloys, no second phase particles can be observed (Fig. 6a and b) which is consistent with higher Al solubility in α-Zn. The larger grain size (19.4 ± 2.8 and 14.4 ± 1.2 μm for 0.5 wt.% and 1wt% Al, respectively) is also consistent with a lack of restriction on grain growth by secondary phases at grain boundaries.

3.2. Texture analysis

(0001) pole figures of the extruded samples are depicted in Fig. 4. Hexagonal close packed (hcp) metals and related alloys with c/a ratios close to the ideal value of 1.633 tend to form basal fiber textures during extrusion, due to the high activity of basal slip systems (Kleiner and Uggowitzer, 2004; Ehsan Mostaed et al., 2015b). Here, as seen in Fig. 4, all samples exhibit textures with basal poles tilted away from normal direction (ND) toward extrusion direction (ED). For hexagonal materials, the c/a ratio alters the activation of the different slip systems. For Mg (c/a = 1.624) basal (0001) $<11\bar{2}0>$ slip results in a sharp basal fiber texture after extrusion. On the other hand in Zn (c/a = 1.856), due to the lower critical resolved shear stress (CRSS) of pyramidal $\{1\ 1\ \bar{2}\ \bar{2}\}$

<11$\bar{2}$3> than prismatic {1 0 $\bar{1}$ 0} <11$\bar{2}$0> slip systems (Solas et al., 2001), a combination of basal and pyramidal slip leads to a texture with basal poles tilted toward ED (Wang and Huang, 2003). Thus, the deformation texture in hcp metals and alloys develops in agreement with the relative contributions from the available deformation paths (basal, prismatic, pyramidal slip and twining systems). Through the deformation processes, the slip plane will gradually rotate toward the extrusion plane and the slip direction toward the ED.

Zn ingot and ST alloys were also subjected to tube extrusion at 300°C with a reduction ratio of 16:1, aimed at producing mini-tubes required for stent manufacturing. The structure of the extruded tubes was evaluated using samples extracted from the die after interrupted extrusion trials, in particular the three regions of a) undeformed region (annealed); b) the transition zone (subjected to increasing deformation as a function of position, toward the higher strain regions) and c) the extruded region (combined effects of high temperature and plastic deformation). Fig. 7 depicts the optical micrographs representative of these regions for all samples. For pure Zn the microstructure is equiaxed in all regions and a small grain refinement occurs during the extrusion, giving grain size of about 280 ± 28.4 μm in the extruded region. In fact, even though the ratio for tube extrusion was much higher than that for billet extrusion (16 vs. 6), the Zn tube possessed coarser grains compared to its billet counterpart (Fig. 7a vs. Fig. 4a) which is due to the higher processing temperature adopted during tube extrusion (300°C vs. 250°C) in combination with a low recrystallization temperature. For all Mg-bearing alloys, a dendritic structure with a network of intermetallic Mg_2Zn_{11} phase along grain boundaries is evident in the undeformed area. In the transition region, due to the initiation of plastic deformation, the original primary Zn dendritic grains became plastically elongated toward the ED, thus forming a lamellar structure. In this region the elongated grains had partially recrystallized and possessed low angle boundary sub-structure. Finally, in the extruded part, due to the higher amount of strain and thereby development of DRX conditions, reasonably fine and equiaxed grains are found. Furthermore, as observed for the extruded billets, Mg_2Zn_{11} phase was broken and distributed almost parallel to the ED. Fig. 8a and b show the EBSD analysis carried out on 0.5 wt.% and 1wt.% Mg-bearing alloy tubes. In comparison with their billet counterpart (see Fig.4c, d), they possess a slightly smaller grain size of 3 ± 0.3 vs. 4.1 ± 0.4 μm and 2.8 ± 0.4 vs 4.4 ± 0.5 μm, respectively, which is ascribed to the significantly higher tube extrusion ratio. Furthermore, (0001) pole figures results show no significant difference in basal texture orientation compared to their billet extruded condition. Hence, it can be stated that, regardless of temperature and extrusion ratio magnitude, tube extruded samples show nearly similar

characteristics in terms of grain size and texture orientation to their billet extrusion counterpart, suggesting that mechanical properties of the tubes could be comparable to those found in the billets.

Interestingly, for Al-containing alloys DRX took place even in the region with lower degree of plastic deformation (the transition region, see Fig. 7e and f), implying that the activation energy needed for DRX in Zn-Al solid solution is lower than that of Zn-Mg alloys. It should be noted that the mean grain size in the 0.5Al and 1Al Zn-bearing alloy tubes was measured to be 70 ± 5.2 and 39 ± 3.6 μm, respectively, which is much bigger than that of extruded billet counterparts. Indeed, as mentioned above, despite higher ratio of tube than billet extrusion, the final microstructure of samples having lower recrystallization temperature (pure Zn, Zn-0.5Al and Zn-1Al) were more affected by temperature than by degree of imposed strain, promoting grain growth in the extruded tube region.

3.2. Mechanical properties

3.2.1. Micro-hardness

Fig. 9a shows the average Vickers micro-hardness of the investigated samples in as-cast and extruded conditions. It is obvious that pure Zn, in both cast and extruded form, has a quite low hardness of about 30 HV. In case of Mg-containing alloys, the hardness is monotonically enhanced with increasing Mg concentration up to 118 HV for the Zn-3Mg alloy. This trend is attributed to the increasing volume fraction of the hard Mg_2Zn_{11} intermetallic phase. For as-cast Zn-0.5Al and Zn-1Al alloys, the hardness increased to 59 and 70 HV, respectively. However, due to the higher solubility of Al in Zn and thereby low second phase volume fraction, Al even at higher content (1wt.%), is less effective in improving the hardness of Zn based alloys. Interestingly, after extrusion no apparent improvement of hardness was observed in any sample, indicating that even strong grain refinement does not influence the hardness of the Zn-based alloys significantly. Fig. 9b depicts micro-hardness profile measurements carried out along the extrusion direction of interrupted tube extrusion test samples. As already observed, for all samples the hardness value from undeformed to extruded region remains nearly constant apart from experimental data scatter, which is due to the local differences in Mg_2Zn_{11} particles. As can be seen, the fluctuation is more striking in case of higher Mg content in which a higher volume fraction of intermetallic particles is present. Moreover, all the tubes show similar hardness values compared to their billet counterparts, confirming that the mechanical properties of the billet and tube extruded samples are rather similar.

3.2.2. Tensile behavior

All the main tensile parameters such as tensile yield stress (YS), ultimate tensile strength (UTS) and elongation to failure (E %) are presented in Fig. 10a. Table 2 also lists the detailed information of the extruded samples including grain size, tensile properties and micro-hardness values. As seen, extruded pure Zn shows very poor TYS and UTS values of 51 MPa and 111 MPa, respectively. The data demonstrate that with increasing Mg concentration, both TYS and UTS consistently increase, ending up to 290 and 400 MPa, respectively, for Zn-3Mg. However, fracture elongation dramatically dropped from 60% to 0.8% moving from pure Zn to Zn-3Mg. This drop is a result of the presence of hard and brittle Mg_2Zn_{11} intermetallic particles, which lead to the easy nucleation and growth of cracks. From Fig. 10a it can be seen that addition of Al also leads to improvement of TYS and UTS to 119 and 203 MPa for Zn-0.5Al, and to 134 and 223 MPa for Zn-1Al, respectively, while keeping remarkably high fracture elongation of 33% and 25%, respectively. Therefore, mechanical properties of Mg-bearing alloys can considerably be improved by the presence of fine and hard Mg_2Zn_{11} intermetallic particles. On the other hand, because of higher solid solubility of Al in Zn, solid solution strengthening is also responsible for improved mechanical properties, especially in Al-containing alloys. In short, the tensile results indicate that in Zn-bearing alloys, Mg is more effective than Al as strengthening alloying element even though it decreases tensile ductility.

Fig. 10b presents the work hardening exponent of the samples, showing that 0.5 wt.% and 1 wt.% Mg have the highest work hardening exponents of 0.22 and 0.34, respectively. Ideally, a vascular stent should be made of a material possessing low yield point, high tensile strength and fairly high work hardening rate in order to avoid strain localization since a radially-expandable stent must undergo significant plastic deformation when expanded into its deployed state. Thus, Fig. 10a and b indicates that the best combination of strength, ductility and work hardening response is achieved by Zn-0.5Mg, providing a promising potential for stent application (Bowen et al., 2013; Mani et al., 2007).

3.3. Fractography

A collection of views of fracture surfaces after tensile testing is displayed in Fig. 11. Extruded pure Zn exhibited typical dimple-fracture features which is consistent with its high elongation to fracture. With increasing Mg content, the number of plastic dimples decreased and evidence of transgranular fracture increased (Fig 11b to e). More precisely, the fracture morphology of 0.15Mg and 0.5Mg alloys show a number

of cleavage planes along with dimples (quasi-cleavage fracture), suggesting a mixed ductile–brittle fracture mode, in good agreement with the tensile test results of Fig.10a. The Zn-1Mg fracture surface is almost fully covered by cleavage planes with only a few dimples, essentially a brittle mode of fracture. At higher Mg concentration, namely Zn-3Mg (Fig. 11e), a different fracture morphology can be seen that is fully transgranular, with eutectic particles on flat fracture facets. Fig. 11f shows the fracture surface of Zn-0.5Al alloy with many uniform and fine dimples separated by sharp ridges, corresponding to the fine equiaxed microstructure and confirming a ductile fracture behavior (as also shown in Fig. 10a). In the case of the Zn-1Al alloy, the number of dimples decreased and some cleavage planes appeared (Fig. 11g), in accordance with the lower tensile elongation to fracture measured in tensile tests.

3.4. Corrosion properties

The corrosion resistance of the as-cast and extruded Zn and Zn-based alloys was evaluated by immersion tests and potentiodynamic polarization measurements. The nature and mechanisms of dissolution of Zn is well-known (Zhang, 2013). The Pourbaix diagram for Zn shows that in acidic environment, no surface oxides of Zn are stable, while under neutral or slightly alkaline conditions (as those in human body) zinc has the tendency to be passivated. It is generally accepted that in neutral and in alkaline solutions the dissolution-passivation of Zn involves a number of intermediate species according to the following reactions (Abd El Aal, 2006; Thomas et al., 2012):

$$Zn + OH^- = Zn(OH)_{ads.} + e \quad (3)$$

$$Zn(OH)_{ads.} + 2OH^- = Zn(OH)_3^- + e \text{ (rds)} \quad (4)$$

$$Zn(OH)_3^- + OH^- = Zn(OH)_4^{2-} \quad (5)$$

$$Zn(OH)_4^{2-} = Zn(OH)_2 + 2OH^- \quad (6)$$

$$Zn + 2OH^- = Zn(OH)_2 + 2e \quad (7)$$

$$Zn + 2OH^- = ZnO + H_2O + 2e \quad (8)$$

Data from average purity Mg (99.95%) are also supplied for comparison (Table 3). The average electrochemical parameters are listed in Table 3 while corrosion rates calculated from Eq. 1 using the measured current densities are shown in Fig. 12. For both as-cast and extruded alloys, the addition of alloying element increases current densities compared to pure Zn, except for the Zn-3Mg alloy where lower current densities and a shifts to a more positive corrosion potential were recorded.

However, the difference between the Zn-X binary alloys and pure Zn is not significant. The improved corrosion resistance of Zn-3Mg alloy can be explained by the formation of Mg_2Zn_{11} phase, dispersed in the Zn matrix (Prosek et al., 2008). The Mg_2Zn_{11} phase is known to have the highest corrosion resistance among Zn-Mg phases (Yao et al., 2015). Moreover, Mg tends to have stabilizing effect on a protective film formed on Zn (Yao et al., 2014). The corrosion rates calculated from corrosion current densities for the investigated alloys are of the same order of magnitude. As listed in Table 3, the corrosion current density i_{corr} decreases as grain size decreases. The electrochemical measurement shows that the corrosion rates of fine-grained extruded Zn alloys are insignificantly lower than those of coarse-grained as-cast ones. It can be attributed to enhanced kinetics of passivation and formation of more robust passive film. The passivation of a surface may be related to the total grain boundary length, which plays an important role in the passivation processes of Zn-based materials (Orlov et al., 2011; Ralston and Birbilis, 2010). The SEM results (Fig. 13) demonstrate that the corrosion products on the extruded alloys are smaller in size and uniformly distributed compared to those of as-cast ones. Moreover, the number of larger and deeper pits seems to be greater in as-cast samples. For extruded samples, pitting damage is reduced significantly and corrosion is more uniform. In case of Zn-Mg binary alloys after extrusion (Figure 13b and c) the size of the second phase particles decreases, suggesting that improved structural homogeneity results in a decrease in the localized corrosion rate. In contrast, Zn-Al alloys exhibit a single phase solid solution microstructure. The elimination of intensive galvanic corrosion is responsible for the more homogenous corrosion properties.

Subsequently, the corrosion resistance of the extruded alloys, as well as pure Zn ingot (Zn-I) and extruded pure zinc (Zn-E) as control materials, was determined by immersion tests. After immersion, samples were analyzed with SEM and EDS to obtain information about the corroded surface and corrosion products. Fig. 14 shows the surface morphology of the Zn-I, the Zn-E and the extruded alloys before and after washing with chromic acid. Samples exposed to Hanks' modified solution for 336 hours exhibit corrosion with some areas covered with layer of corrosion products while other are nearly impassive.

The corrosion morphology of Zn-I is typical of a localized corrosion mode. The corrosion products are clustered in specific areas, while the parts of the specimen where corrosion does not occur retain a bright metallic lustre. In case of fine-grained Zn-E, a granular corrosion deposit is distributed homogenously on the surface. After removal of the corrosion products, the pits developed during the immersion on the surface of Zn-I are revealed to be significantly larger and deeper than those on Zn-E, confirming that the corrosion rate of Zn-E

is lower than Zn-I (see Fig.15). This is in agreement with other studies where corrosion rates have been reported to decrease with decreasing grain size (Orlov et al., 2011; Ralston and Birbilis, 2010), due to the ability of grain boundaries to passivate more readily.

Corrosion of Zn-0.15Mg, Zn-0 .5Mg and Zn-1Mg is clearly non-uniform, showing noticeable micro-galvanic activity between metal matrix and precipitates segregated along the extrusion direction. Localized corrosion can rapidly reduce mechanical integrity, which might induce the failure of an implant during degradation. Micro-galvanic effects depend upon the size and distribution of local anodes (Mg-rich phases) and cathodes (Zn matrix); smaller and closer local electrodes reduce the overall pH of the samples. This is evident in Fig. 14 from the distribution and size of local anodic corrosion attacks on the different samples. It can be seen that after removing corrosion products, the formation of galvanic micro-cells between Zn and Mg-rich phases results in many deep pits formed on the surface.

Zn-3Mg alloy possess the best corrosion resistance among the samples investigated here. In particular the extruded Zn-3Mg alloy, with a uniform and homogenously dispersed second phase, tends to form a uniform protective layer of Mg-containing corrosion products that retard localized corrosion.

The Zn-Al alloys have a superior corrosion resistance to multiphase Zn-Mg alloys, because the absence of second phases eliminates the galvanic reactions that accelerate corrosion (see Fig. 14g and h). The morphology of the corroded surface looks uniform and the depth of the corroded areas is relatively shallow. The formation of more compact and homogenous surface films are suggested to be responsible for better corrosion properties.

EDS analyses of the surface corrosion products after immersion tests (Table 4) show Zn, P, O, C, Cl, Mg and Ca. It can be assumed that degradation products contain calcium phosphates and carbonates (Gong et al., 2015; Vojtěch et al., 2011) and the oxygen content may imply the precipitation of oxides and insoluble hydroxides. This is probably a result of the ionic interaction between Zn corrosion products and diverse acid radicals such as: $Cl^{-}, HCO_3^{-}, HPO_4^{2-}$ in Hanks' modified solution (Lévesque et al., 2008). For example, the formation of zinc carbonates can occur according to the following reactions (Zhang, 2013):

$$ZnO + 2H^{+} \leftrightarrow Zn^{2+} + H_2O \quad (9)$$

$$Zn^{2+} + H_2CO_3 \leftrightarrow ZnCO_{3(s)} + 2H^{+} \quad (10)$$

In the presence of Cl^-, Zn^{2+} may be able to form various soluble species, such as $ZnCl_2$, $ZnCl_2^-$ and surface-confined $\beta - ZnOHCl$ that can lead to the formation of the main product of zinc hydroxychloride, $Zn_5(OH)_8Cl_2$. Nevertheless, it has been reported that the presence of HPO_4^{2-} ions inhibits dissolution of Zn, forming insoluble phosphates such as $ZnHPO_4$. Furthermore, intermediate corrosion products, which are formed on the surface of the specimen, can prevent direct exposure to the environment. In particular, $Zn_5(OH)_8Cl_2 \cdot H_2O$ (simonkolleite) contributes to the improvement of corrosion resistance. It has been reported that the formation of simonkolleite is a reversible reaction in a solution containing Cl^- ions (Falk et al., 1998):

$$5ZnO + 2Cl^- + 6H_2O \leftrightarrow Zn_5(OH)_8Cl_2H_2O + 2OH^- \cdot 5ZnO$$

$$+2Cl^- + 6H_2O \leftrightarrow Zn_5(OH)_8Cl_2 \cdot 2H_2O + 2OH^- \quad (11)$$

Subsequently, the OH^- are neutralized, and magnesium hydroxyl carbonate may be formed as follows:

$$2Mg^{2+} + 2OH^- + CO_2^{2-} \rightarrow Mg_2(OH)_2CO_3 \quad (12)$$

Magnesium may improve corrosion resistance by the formation of Mg-containing electrochemically inert species such as $Mg_2(OH)_2CO_3$. on the surface. A Mg-containing form of simonkolleite has been reported to act as a corrosion barrier (Yao et al., 2014). A similar effect may occur in case of Al-containing Zn alloys, if incorporation of aluminum into the corrosion product retards corrosion due to the protective effect of the insoluble degradation layer (Hosking et al., 2007).

3.5. Mechanical integrity

The Zn binary alloys investigated here clearly show suitable properties for medical implant applications. However, a deterioration in mechanical integrity is expected as degradation progresses and has to be measured. Moreover, any mechanical loads may accelerate this process due to the dual effect of corrosion and stress, leading to premature cracking. Zn-based alloys in weight-bearing implants would require sufficient strength for the duration of the service period and for all applications it is important that implants keep their strength at least until the damaged tissue heals. To evaluate the effect of corrosion on mechanical properties, compression tests were carried out on the samples before and after immersion. Fig. 16 compares the compressive yield strength (CYS) of the samples before and after immersion in Hanks' modified solution for 336 hours. The calculated reduction of CYS values are listed in Table 5. The data are of major importance for the evaluation of residual

strength of bio devices after partial degradation. In order to have a better understanding of Mg and Zn mechanical integrity, AZ31 Mg alloy was also chosen for this test since it is proved that it possesses good strength and ductility. As seen in Fig 11, for the non-immersed samples, CYS increases with increasing Mg content from 75 MPa to 495 MPa for pure Zn and Zn-3Mg, respectively. Al is less effective in improving CYS, giving 112 MPa and 154 MPa for Zn-0.5Al and Zn-1Al, respectively, in agreement with tensile tests already discussed (Fig. 10a).

For all the samples CYS decreases after immersion, although the amount varies between alloys. Table 5 shows that increasing Mg from 0.15 wt.% to 1 wt.% gives larger reductions of CYS, from 8.7 % to 20%, respectively, due to the increased volume fraction and non-uniform distribution of second phase particles. For the eutectic alloy, however, the reduction dropped to 8.3%, similar to that measured for pure Zn. This is probably due to localized galvanic corrosion, which decreases the load-bearing capacity by concentrating stresses around pits. In case of Al-containing alloys, CYS reductions of 8.7 and 11.2 %, were measured for 0.5 wt.% and 1 wt.% Al, indicating the lower rate of loss of mechanical integrity compared to Mg-bearing hypoeutectic alloys due to the presence of Al in the solute form, minimizing the localized corrosion effect. Thus, it can be stated that, although Al-bearing alloys along with Zn-3Mg exhibit the lowest rate of loss of mechanical integrity among all the investigated samples, toxicity related concerns for Zn-Al alloys and lack of ductility for Zn-3Mg restrict them from biodegradable stent applications. From Table 5, and taking tensile strength, ductility and work hardenability into account, Zn-0.5Mg alloy best fulfills the requirements for cardiovascular stent applications. Nevertheless, the AZ31 alloy has ~45% reduction of CYS after immersion, which is outperformed by all the Zn-based alloys investigated here and confirms their great potential as a new generation of biodegradable metallic stents.

3.6. Laser cutting

For stent manufacturing, laser cutting represents the industrially accepted method for producing stents starting from the extruded mini-tubes. Thus, the final microstructure of a laser cut stent is of paramount importance affecting the stent's local microstructure, hence mechanical and corrosion properties. The load-bearing structure of a vascular stent consists of a very small cross section, roughly 200×200 μm^2. Crystal grain sizes of tens of micrometers would lead to a limited number of slip plane orientations and anisotropic mechanical properties. In contrast, a fine microstructure would occupy the same volume with a large number of grains, minimizing the

random orientation effects and producing a more isotropic behavior. Thus, grain growth during any thermal processing is important. In order to investigate thermal effects induced by laser processing a small rectangular piece was cut by laser from a Zn-0.5Mg alloy tube, as depicted in Fig.17a and b. The microstructure next to the cut edge was characterized using EBSD. Limited amount of dross is visible on the tube surface (Fig. 17a), whereas, the cut kerf is characterized by a molten layer with surface striations. In absence of excessive dross and molten layer, such a cut kerf is feasible for consecutive chemical and electrochemical polishing steps (Demir et al., 2013). Fig. 17c shows an IPF map in the vicinity of the laser cut edge (as marked in red in Fig. 17b). From comparison with Fig. 8a it is clear that a few micrometers from the cut edge there is just a slight change of the microstructure, with a mean grain size of 3.3 ± 0.4 μm, showing that no significant thermal effects on microstructure or grain growth were generated by laser processing (Fig. 17d). Furthermore, the texture orientation (Fig. 17e) of the laser processed Zn-0.5Mg remained unchanged.

The use of the ns-pulsed laser provides reduced thermal interaction compared to the continuous wave (CW) ones, commonly used in the cutting of permanent stents in stainless steel or Co-Cr alloys. Moreover, the use of CW lasers can induce larger amount of dross on materials with low melting point such as Mg alloys (Demir and Previtali, 2014). Going towards shorter pulse durations, namely fs-pulsed lasers the thermal interaction with cut material can be avoided completely. As confirmed previously on ultrafine-grained Mg alloys, which constitutes another example of heat sensitive material (Ge et al., 2013), ns-pulsed laser cutting is effective in avoiding heat damage on Mg-Zn alloys. This fact also improves industrial viability in producing Zn-alloy stents, since the investment and operation costs can be reduced compared to a fs-pulsed system. Generally, the grain size and texture close to the cut surface are comparable to that of the untreated material, suggesting that the mechanical behavior of an Zn-Mg alloy stent would be similar to its tube counterpart. The cut kerf characterized by molten layer, which is expected to have in chemical and microstructural variations, is eliminated by the successive cleaning steps.

4. Conclusion

In this study, Zn–based binary alloys with different concentrations of Mg and Al as alloying elements have been investigated as possible candidates for biodegradable stent applications. All materials were cast into billets at 500°C and solution-heated (48 hours at 350°C), followed by hot extrusion either at 250°C with an extrusion

ratio of 6:1 to produce cylindrical rods, or at 300°C with ratio of 16:1 to produce tubes with an outer diameter of 4mm. Based on the results obtained, the following conclusions can be made:

- Hot extrusion of Zn-Mg alloys produced a fine equiaxed grain structure that was a mixture of α-Zn and Mg_2Zn_{11} segregated to grain boundaries. The final grain size of the alloys decreased with increasing Mg content, although additions above 0.5 wt.% had only a minor effect on grain size. A similar treatment of Zn-Al alloys produced a single phase microstructure (due to the higher solubility of Al in Zn) and coarser grains.
- Hot tube extrusion led to a considerable grain refinement in all the investigated alloys. An EBSD study found similar grain size and texture orientation in both extruded tubes and rods, indicating comparable mechanical properties.
- EBSD analysis showed that, in contrast to Mg alloys, extruded Zn-based alloys exhibited textures with (0001) tilted a few degrees from the extrusion direction.
- Increasing the Mg content improved micro-hardness and tensile strength of the Zn-Mg alloys due to the increasing volume fraction of the hard Mg_2Zn_{11} intermetallic phase. However, a corresponding decrease in ductility also occurred.
- Al has a smaller effect on mechanical properties than Mg since it has higher solubility in Zn, leading to single phase structure even at higher content (1 wt.%).
- Among all the investigated alloys, Zn-0.5 wt.% Mg has the best combination of strength and ductility, giving the most promise for stent application.
- Corrosion rates were measured by potentiodynamic polarization and static immersion tests (using Hanks' modified solution). The corrosion rates of Zn and Zn-based alloys, both as-cast and extruded conditions, were in the same order of magnitude. Extruded alloys exhibited slightly superior corrosion resistance and a slower degradation ratio than those of their cast counterparts.
- A shift of corrosion regime from localized pitting to a more uniform corrosion mode was observed in the fine-grained alloys, mainly due to second phase refinement as well as the formation of a more compacted passive layer on their surface.
- These properties show that Zn-Mg extruded alloys may be excellent biodegradable materials owing to a good combination of mechanical performance and degradation rate.

- A study of mechanical integrity during degradation indicated that increasing Mg from 0.15 to 1wt.% led to larger drops in compressive yield stress, 8.7% and 20% respectively. This effect is attributed to the increased volume fraction of the second phase, resulting in more local galvanic corrosion pitting. Zn-Al alloys had a slower loss of mechanical integrity, a result of the higher solubility of Al and a lack of second phase particles.
- An EBSD analysis of a laser cut Zn-0.5Mg hot-extruded tube found that neither grain coarsening nor texture modification occurred close to the laser cut edge. It is therefore expected that a cut stent would have comparable mechanical properties to those of uncut material.

References

Abd El Aal, E.E., 2006. Factors affecting the anodic behaviour of zinc electrode in borate solutions. Corros. Sci. 48, 343–360. doi:10.1016/j.corsci.2005.01.003

Al-Abdullat, Y., Tsutsumi, S., Nakajima, N., Ohta, M., Kuwahara, H., Ikeuchi, K., 2001. Surface Modification of Magnesium by NaHCO3 and Corrosion Behavior in Hank's solution for New Biomaterial Applications. Mater. Trans. 42, 1777–1780. doi:10.2320/matertrans.42.1777

ASTM E8-04, 2004. Test Methods for Tension Testing of Metallic Materials. Annual book of ASTM standards.

ASTM E9-09, 2009. Test Methods of Compression Testing of Metallic Materials at Room Temperature. Annual book of ASTM standards.

ASTM G31-72 Standard Practice for Laboratory Immersion Corrosion Testing of Metals, n.d.

ASTM G59-97 Standard Test Method for Conducting Potentiodynamic Polarization Resistance Measurements, 2003.

Babic, M., Mitrovic, S., Jeremic, B., 2010. The influence of heat treatment on the sliding wear behavior of a ZA-27 alloy. Tribol. Int. 43, 16–21. doi:10.1016/j.triboint.2009.04.016

Bowen, P.K., Drelich, J., Goldman, J., 2013. Zinc Exhibits Ideal Physiological Corrosion Behavior for Bioabsorbable Stents. Adv. Mater. 25, 2577–2582. doi:10.1002/adma.201300226

Bowen, P.K., Guillory II, R.J., Shearier, E.R., Seitz, J.-M., Drelich, J., Bocks, M., Zhao, F., Goldman, J., 2015. Metallic zinc exhibits optimal biocompatibility for bioabsorbable endovascular stents. Mater. Sci. Eng. C 56, 467–472. doi:10.1016/j.msec.2015.07.022

Butts, D.A., Gale, W.F., 2004. 11 - Equilibrium diagrams, in: Totemeier, W.F.G.C. (Ed.), Smithells Metals Reference Book (Eighth Edition). Butterworth-Heinemann, Oxford, pp. 1–534.

Cheng, J., Liu, B., Wu, Y.H., Zheng, Y.F., 2013. Comparative invitro study on pure metals (Fe, Mn, Mg, Zn and W) as biodegradable metals. J. Mater. Sci. Technol. 29, 619–627. doi:10.1016/j.jmst.2013.03.019

Demir, A.G., khan, Previtali, B., Biffi, C.A., 2013. Fibre Laser Cutting and Chemical Etching of AZ31 for Manufacturing Biodegradable Stents. Adv. Mater. Sci. Eng. 2013, e692635. doi:10.1155/2013/692635

Demir, A.G., Previtali, B., 2014. Comparative study of CW, nanosecond- and femtosecond-pulsed laser microcutting of AZ31 magnesium alloy stents. Biointerphases 9, 029004. doi:10.1116/1.4866589

Di Mario, C., Griffiths, H., Goktekin, O., Peeters, N., Verbist, J., Bosiers, M., Deloose, K., Heublein, B., Rohde, R., Kasese, V., Ilsley, C., Erbel, R., 2004. Drug-Eluting Bioabsorbable Magnesium Stent. J. Intervent. Cardiol. 17, 391–395. doi:10.1111/j.1540-8183.2004.04081.x

Erbel, R., Di Mario, C., Bartunek, J., Bonnier, J., de Bruyne, B., Eberli, F.R., Erne, P., Haude, M., Heublein, B., Horrigan, M., Ilsley, C., Böse, D., Koolen, J., Lüscher, T.F., Weissman, N., Waksman, R., 2007. Temporary scaffolding of coronary arteries with bioabsorbable magnesium stents: a prospective, non-randomised multicentre trial. The Lancet 369, 1869–1875. doi:10.1016/S0140-6736(07)60853-8

Falk, T., Svensson, J.-E., Johansson, L.-G., 1998. The Influence of CO 2 and NaCl on the Atmospheric Corrosion of Zinc A Laboratory Study. J. Electrochem. Soc. 145, 2993–2999. doi:10.1149/1.1838753

Freeman, J., 1926. Pure Zinc at normal and elevated temperatures. National Bureau of Standards.

Ge, Q., Dellasega, D., Demir, A.G., Vedani, M., 2013. The processing of ultrafine-grained Mg tubes for biodegradable stents. Acta Biomater., Biodegradable Metals 9, 8604–8610. doi:10.1016/j.actbio.2013.01.010

Gong, H., Wang, K., Strich, R., Zhou, J.G., 2015. In vitro biodegradation behavior, mechanical properties, and cytotoxicity of biodegradable Zn–Mg alloy. J. Biomed. Mater. Res. B Appl. Biomater. n/a–n/a. doi:10.1002/jbm.b.33341

Gu, X.N., Zhou, W.R., Zheng, Y.F., Cheng, Y., Wei, S.C., Zhong, S.P., Xi, T.F., Chen, L.J., 2010. Corrosion fatigue behaviors of two biomedical Mg alloys – AZ91D and WE43 – In simulated body fluid. Acta Biomater. 6, 4605–4613. doi:10.1016/j.actbio.2010.07.026

Gu, X., Zheng, Y., Cheng, Y., Zhong, S., Xi, T., 2009. In vitro corrosion and biocompatibility of binary magnesium alloys. Biomaterials 30, 484–498. doi:10.1016/j.biomaterials.2008.10.021

Hermawan, H., Dubé, D., Mantovani, D., 2010. Degradable metallic biomaterials: Design and development of Fe–Mn alloys for stents. J. Biomed. Mater. Res. A 93A, 1–11. doi:10.1002/jbm.a.32224

Hosking, N.C., Ström, M.A., Shipway, P.H., Rudd, C.D., 2007. Corrosion resistance of zinc–magnesium coated steel. Corros. Sci. 49, 3669–3695. doi:10.1016/j.corsci.2007.03.032

Kleiner, S., Uggowitzer, P.J., 2004. Mechanical anisotropy of extruded Mg–6% Al–1% Zn alloy. Mater. Sci. Eng. A 379, 258–263. doi:10.1016/j.msea.2004.02.020

Lastra, M.D., Pastelin, R., Camacho, A., Monroy, B., Aguilar, A.E., 2001. Zinc intervention on macrophages and lymphocytes response. J. Trace Elem. Med. Biol. 15, 5–10. doi:10.1016/S0946-672X(01)80019-5

Lévesque, J., Hermawan, H., Dubé, D., Mantovani, D., 2008. Design of a pseudo-physiological test bench specific to the development of biodegradable metallic biomaterials. Acta Biomater. 4, 284–295. doi:10.1016/j.actbio.2007.09.012

Li, H., Yang, H., Zheng, Y., Zhou, F., Qiu, K., Wang, X., 2015. Design and characterizations of novel biodegradable ternary Zn-based alloys with IIA nutrient alloying elements Mg, Ca and Sr. Mater. Des. 83, 95–102. doi:10.1016/j.matdes.2015.05.089

Li, L., Gao, J., Wang, Y., 2004. Evaluation of cyto-toxicity and corrosion behavior of alkali-heat-treated magnesium in simulated body fluid. Surf. Coat. Technol. 185, 92–98. doi:10.1016/j.surfcoat.2004.01.004

Liu, L., Chen, X., Pan, F., Wang, Z., Liu, W., Cao, P., Yan, T., Xu, X., 2015. Effect of Y and Ce additions on microstructure and mechanical properties of Mg–Zn–Zr alloys. Mater. Sci. Eng. A 644, 247–253. doi:10.1016/j.msea.2015.07.065

Liu, X., Sun, J., Yang, Y., Pu, Z., Zheng, Y., 2015. In vitro investigation of ultra-pure Zn and its mini-tube as potential bioabsorbable stent material. Mater. Lett. 161, 53–56. doi:10.1016/j.matlet.2015.06.107

Li, Z., Gu, X., Lou, S., Zheng, Y., 2008. The development of binary Mg–Ca alloys for use as biodegradable materials within bone. Biomaterials 29, 1329–1344. doi:10.1016/j.biomaterials.2007.12.021

Mani, G., Feldman, M.D., Patel, D., Agrawal, C.M., 2007. Coronary stents: A materials perspective. Biomaterials 28, 1689–1710. doi:10.1016/j.biomaterials.2006.11.042

McCall, K.A., Huang, C., Fierke, C.A., 2000. Zinc and health: Current status and future directions. J Nutr 22, 1437–1446.

Mm, El.-Omar., Dangas. G, Iakovou. I, Mehran. R, 2001. Update on In-stent Restenosis. Curr. Interv. Cardiol. Rep. 3, 296–305.

Mostaed, E., Fabrizi, A., Bonollo, F., Vedani, M., 2015. Microstructural, texture, plastic anisotropy and superplasticity development of ZK60 alloy during equal channel angular extrusion processing. Metall. Ital. 107, 5–12.

Mostaed, E., Fabrizi, A., Dellasega, D., Bonollo, F., Vedani, M., 2015a. Microstructure, mechanical behavior and low temperature superplasticity of ECAP processed ZM21 Mg alloy. J. Alloys Compd. 638, 267–276. doi:10.1016/j.jallcom.2015.03.029

Mostaed, E., Fabrizi, A., Dellasega, D., Bonollo, F., Vedani, M., 2015b. Grain size and texture dependence on mechanical properties, asymmetric behavior and low temperature superplasticity of ZK60 Mg alloy. Mater. Charact. 107, 70–78. doi:10.1016/j.matchar.2015.06.009

Mostaed, E., Ge, Q., Vedani, M., De Oliveira Botelho, P.A., Zanella, C., Deflorian, F., 2013. Investigation on the influence of grain size on strength, ductility, and corrosion properties in Mg and Mg-Zn based alloys for biodegradable stents. Eur. Cell. Mater. 26, 84.

Mostaed, E., Hashempour, M., Fabrizi, A., Dellasega, D., Bestetti, M., Bonollo, F., Vedani, M., 2014a. Microstructure, texture evolution, mechanical properties and corrosion behavior of ECAP processed ZK60 magnesium alloy for biodegradable applications. J. Mech. Behav. Biomed. Mater. 37, 307–322. doi:10.1016/j.jmbbm.2014.05.024

Mostaed, E., Vedani, M., Hashempour, M., Bestetti, M., 2014b. Influence of ECAP process on mechanical and corrosion properties of pure Mg and ZK60 magnesium alloy for biodegradable stent applications. Biomatter 4, e28283. doi:10.4161/biom.28283

Murni, N.S., Dambatta, M.S., Yeap, S.K., Froemming, G.R.A., Hermawan, H., 2015. Cytotoxicity evaluation of biodegradable Zn–3Mg alloy toward normal human osteoblast cells. Mater. Sci. Eng. C 49, 560–566. doi:10.1016/j.msec.2015.01.056

Ogushi, Y., Mostaed, E., Dellasega, D., Vedani, M., Miyamoto, H., Fujiwara, H., 2014. Aging behavior of ECAP processed AZ80 Mg alloy. IOP Conf. Ser. Mater. Sci. Eng. 63, 012076. doi:10.1088/1757-899X/63/1/012076

Onuma, Y., Ormiston, J., Serruys, P.W., 2011. Bioresorbable Scaffold Technologies. Circ. J. 75, 509–520. doi:10.1253/circj.CJ-10-1135

Orlov, D., Ralston, K.D., Birbilis, N., Estrin, Y., 2011. Enhanced corrosion resistance of Mg alloy ZK60 after processing by integrated extrusion and equal channel angular pressing. Acta Mater. 59, 6176–6186. doi:10.1016/j.actamat.2011.06.033

Pandey, J.P., Prasad, B.K., Yegneswaran, A.H., 1998. Dry Sliding Wear Behaviour of a Zinc-Based Alloy: A Comparative Study with a Leaded-Tin Bronze. Mater. Trans. JIM 39, 1121–1125. doi:10.2320/matertrans1989.39.1121

Pan, H., Qin, G., Xu, M., Fu, H., Ren, Y., Pan, F., Gao, Z., Zhao, C., Yang, Q., She, J., Song, B., 2015. Enhancing mechanical properties of Mg–Sn alloys by combining addition of Ca and Zn. Mater. Des. 83, 736–744. doi:10.1016/j.matdes.2015.06.032

Park, S.H., Kim, S.-H., Kim, Y.M., You, B.S., 2015. Improving mechanical properties of extruded Mg–Al alloy with a bimodal grain structure through alloying addition. J. Alloys Compd. 646, 932–936. doi:10.1016/j.jallcom.2015.06.034

Peuster, M., Hesse, C., Schloo, T., Fink, C., Beerbaum, P., von Schnakenburg, C., 2006. Long-term biocompatibility of a corrodible peripheral iron stent in the porcine descending aorta. Biomaterials 27, 4955–4962. doi:10.1016/j.biomaterials.2006.05.029

Peuster, M., Wohlsein, P., Brügmann, M., Ehlerding, M., Seidler, K., Fink, C., Brauer, H., Fischer, A., Hausdorf, G., 2001. A novel approach to temporary stenting: degradable cardiovascular stents produced from corrodible metal—results 6–18 months after implantation into New Zealand white rabbits. Heart 86, 563–569. doi:10.1136/heart.86.5.563

Pierson, D., Edick, J., Tauscher, A., Pokorney, E., Bowen, P., Gelbaugh, J., Stinson, J., Getty, H., Lee, C.H., Drelich, J., Goldman, J., 2012. A simplified in vivo approach for evaluating the bioabsorbable behavior of candidate stent materials. J. Biomed. Mater. Res. - Part B Appl. Biomater. 100 B, 58–67. doi:10.1002/jbm.b.31922

Plum, L.M., Rink, L., Haase, H., 2010. The Essential Toxin: Impact of Zinc on Human Health. Int. J. Environ. Res. Public. Health 7, 1342–1365. doi:10.3390/ijerph7041342

Prosek, T., Nazarov, A., Bexell, U., Thierry, D., Serak, J., 2008. Corrosion mechanism of model zinc–magnesium alloys in atmospheric conditions. Corros. Sci. 50, 2216–2231. doi:10.1016/j.corsci.2008.06.008

Pürçek, G., Savaşkan, T., Küçükömeroğlu, T., Murphy, S., 2002. Dry sliding friction and wear properties of zinc-based alloys. Wear 252, 894–901. doi:10.1016/S0043-1648(02)00050-9

Qiang, G., Mostaed, E., Zanella, C., Zhentao, Y., Vedani, M., 2014. Ultra-Fine Grained Degradable Magnesium for Biomedical Applications. Rare Met. Mater. Eng. 43, 2561–2566. doi:10.1016/S1875-5372(15)60001-7

Ralston, K.D., Birbilis, N., 2010. Effect of Grain Size on Corrosion: A Review. Corrosion 66, 075005–075005–13. doi:10.5006/1.3462912

Robson, J.D., Henry, D.T., Davis, B., 2009. Particle effects on recrystallization in magnesium–manganese alloys: Particle-stimulated nucleation. Acta Mater. 57, 2739–2747. doi:10.1016/j.actamat.2009.02.032

Saltman, P.D., Strause, L.G., 1993. The role of trace minerals in osteoporosis. J. Am. Coll. Nutr. 12, 384–389. doi:10.1080/07315724.1993.10718327

Savaskan, T., Murphy, S., 1987. Mechanical properties and lubricated wear of Zn-25Al-based alloys. Wear 116, 211–224. doi:10.1016/0043-1648(87)90234-1

Solas, D.E., Tomé, C.N., Engler, O., Wenk, H.R., 2001. Deformation and recrystallization of hexagonal metals: modeling and experimental results for zinc. Acta Mater. 49, 3791–3801. doi:10.1016/S1359-6454(01)00261-0

Song, G., 2007. Control of biodegradation of biocompatable magnesium alloys. Corros. Sci. 49, 1696–1701. doi:10.1016/j.corsci.2007.01.001

Thomas, S., Birbilis, N., Venkatraman, M. s., Cole, I. s., 2012. Corrosion of Zinc as a Function of pH. Corrosion 68, 015009–1. doi:10.5006/1.3676630

Tong, L.B., Zhang, Q.X., Jiang, Z.H., Meng, J., Zhang, H.J., 2015. Enhanced mechanical properties of extruded Mg–Y–Zn alloy fabricated via low-strain rolling. Mater. Sci. Eng. A 620, 483–489. doi:10.1016/j.msea.2014.10.005

Törne, K., Larsson, M., Norlin, A., Weissenrieder, J., 2015. Degradation of zinc in saline solutions, plasma, and whole blood. J. Biomed. Mater. Res. B Appl. Biomater. doi:10.1002/jbm.b.33458

TRUMBO, P., YATES, A.A., SCHLICKER, S., POOS, M., 2001. Dietary Reference Intakes: Vitamin A, Vitamin K, Arsenic, Boron, Chromium, Copper, Iodine, Iron, Manganese, Molybdenum, Nickel, Silicon, Vanadium, and Zinc. J. Am. Diet. Assoc. 101, 294–301. doi:10.1016/S0002-8223(01)00078-5

Vojtěch, D., Kubásek, J., Šerák, J., Novák, P., 2011. Mechanical and corrosion properties of newly developed biodegradable Zn-based alloys for bone fixation. Acta Biomater. 7, 3515–3522. doi:10.1016/j.actbio.2011.05.008

Wang, L., Mostaed, E., Cao, X., Huang, G., Fabrizi, A., Bonollo, F., Chi, C., Vedani, M., 2016. Effects of texture and grain size on mechanical properties of AZ80 magnesium alloys at lower temperatures. Mater. Des. 89, 1–8. doi:10.1016/j.matdes.2015.09.153

Wang, Y.N., Huang, J.C., 2003. Texture analysis in hexagonal materials. Mater. Chem. Phys. 81, 11–26. doi:10.1016/S0254-0584(03)00168-8

Witte, F., Hort, N., Vogt, C., Cohen, S., Kainer, K.U., Willumeit, R., Feyerabend, F., 2008. Degradable biomaterials based on magnesium corrosion. Curr. Opin. Solid State Mater. Sci. 12, 63–72. doi:10.1016/j.cossms.2009.04.001

Witte, F., Kaese, V., Haferkamp, H., Switzer, E., Meyer-Lindenberg, A., Wirth, C.J., Windhagen, H., 2005. In vivo corrosion of four magnesium alloys and the associated bone response. Biomaterials 26, 3557–3563. doi:10.1016/j.biomaterials.2004.09.049

Xu, L., Yu, G., Zhang, E., Pan, F., Yang, K., 2007. In vivo corrosion behavior of Mg-Mn-Zn alloy for bone implant application. J. Biomed. Mater. Res. A 83A, 703–711. doi:10.1002/jbm.a.31273

Yao, C., Tay, S.L., Zhu, T., Shang, H., Gao, W., 2015. Effects of Mg content on microstructure and electrochemical properties of Zn–Al–Mg alloys. J. Alloys Compd. 645, 131–136. doi:10.1016/j.jallcom.2015.05.010

Yao, C., Wang, Z., Tay, S.L., Zhu, T., Gao, W., 2014. Effects of Mg on microstructure and corrosion properties of Zn–Mg alloy. J. Alloys Compd. 602, 101–107. doi:10.1016/j.jallcom.2014.03.025

Zeng, R., Kainer, K.U., Blawert, C., Dietzel, W., 2011. Corrosion of an extruded magnesium alloy ZK60 component - The role of microstructural features. J. Alloys Compd. 509, 4462–4469. doi:10.1016/j.jallcom.2011.01.116

Zhang, X.G., 2013. Corrosion and Electrochemistry of Zinc. Springer Science & Business Media.

Figures:

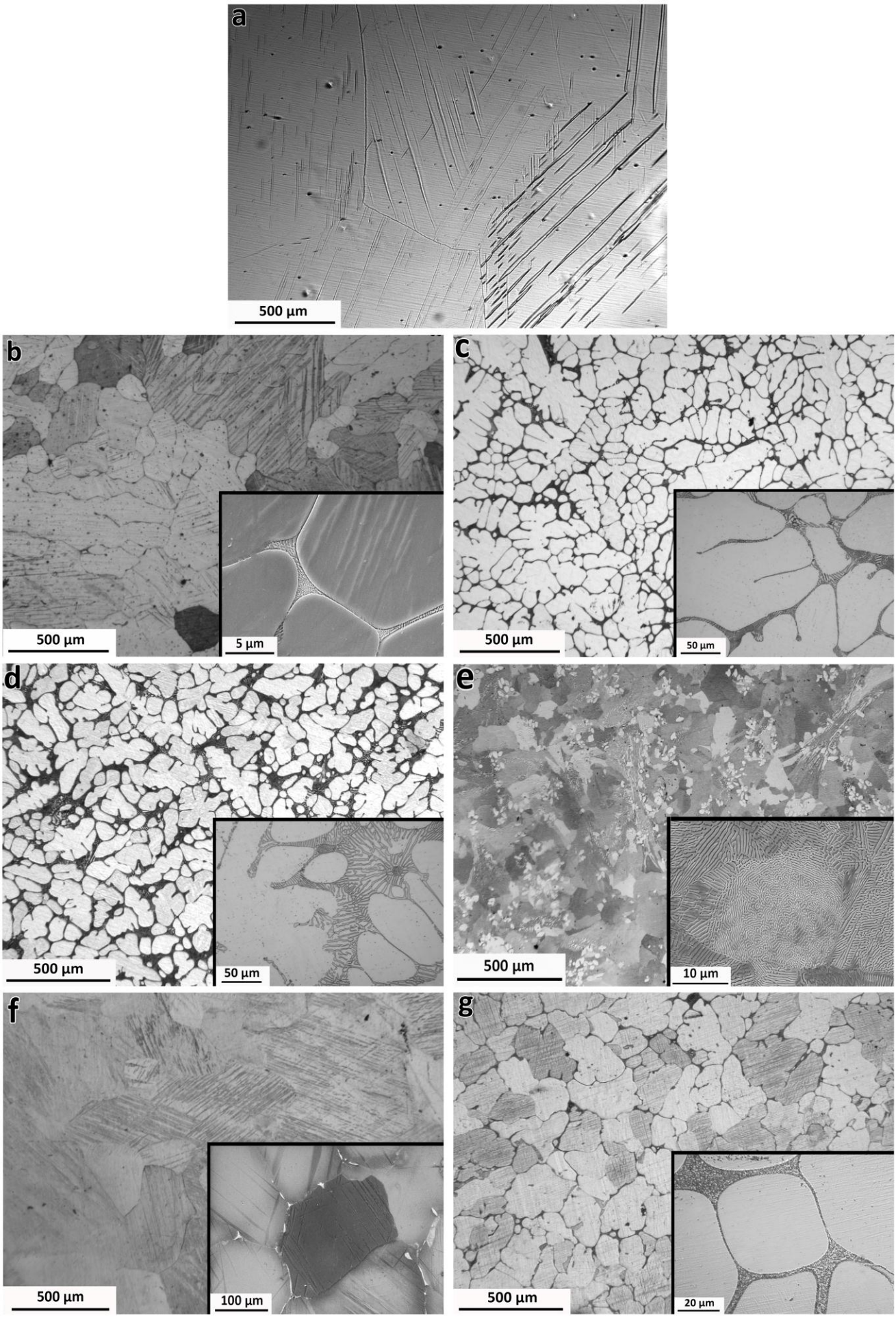
a
500 µm
b
500 µm
5 µm
c
500 µm
50 µm
d
500 µm
50 µm
e
500 µm
10 µm
f
500 µm
100 µm
g
500 µm
20 µm

Fig. 1. Microstructure of the investigated samples in the as-cast condition: (a) Zn, (b) Zn-0.15Mg, (c) Zn-0.5Mg, (d) Zn-1Mg, (e) Zn-3Mg (f) Zn-0.5Al and (g) Zn-1Al alloys.

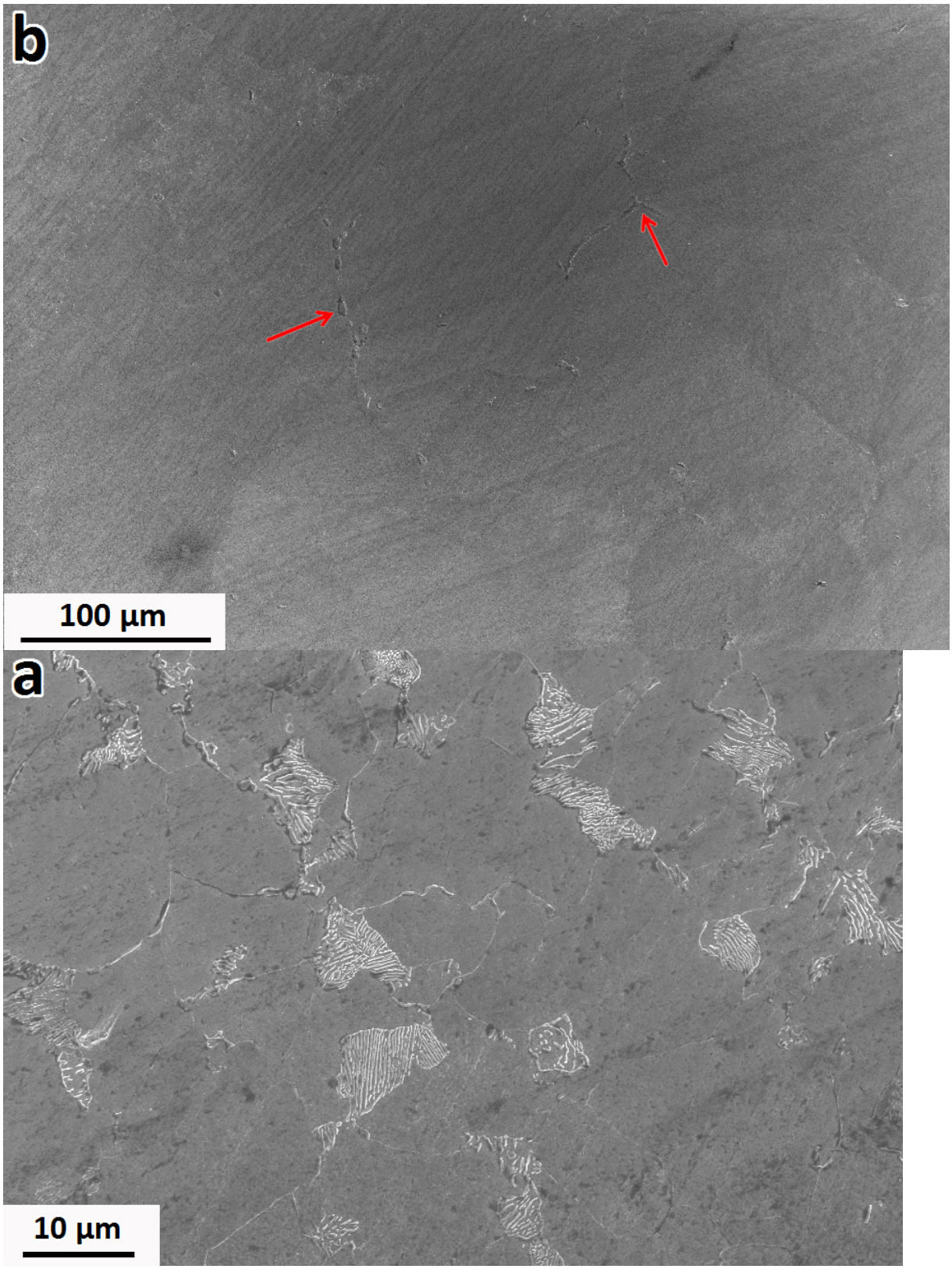

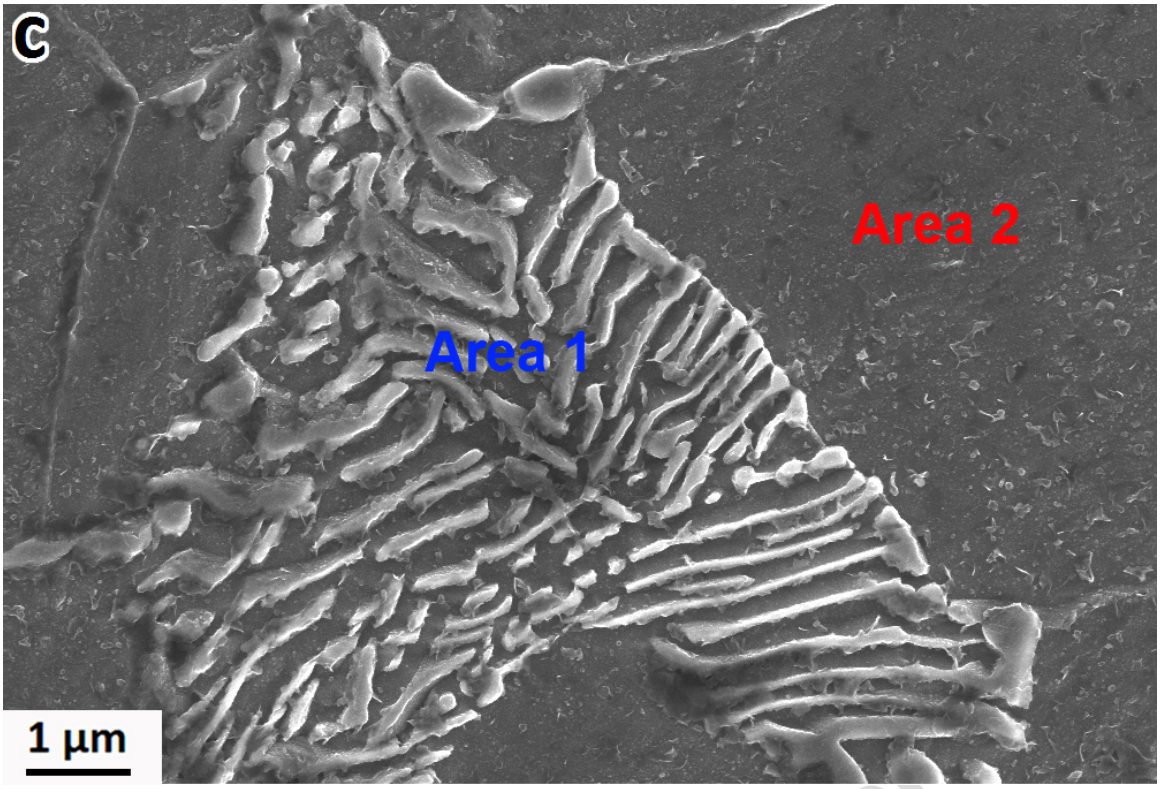

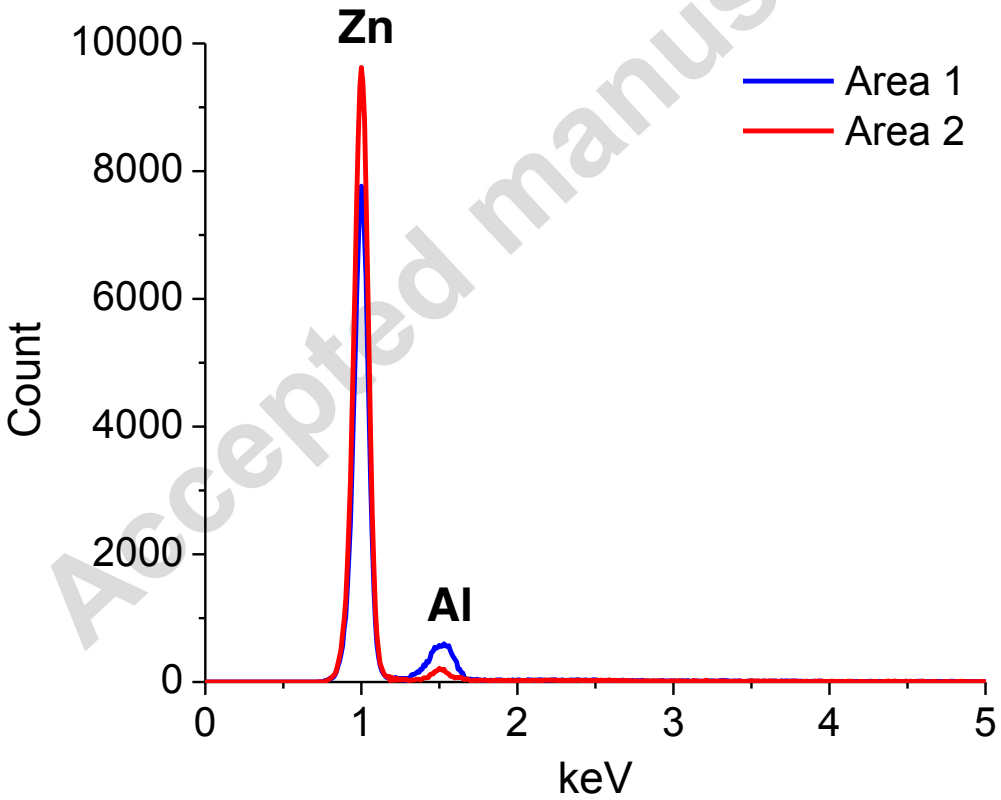

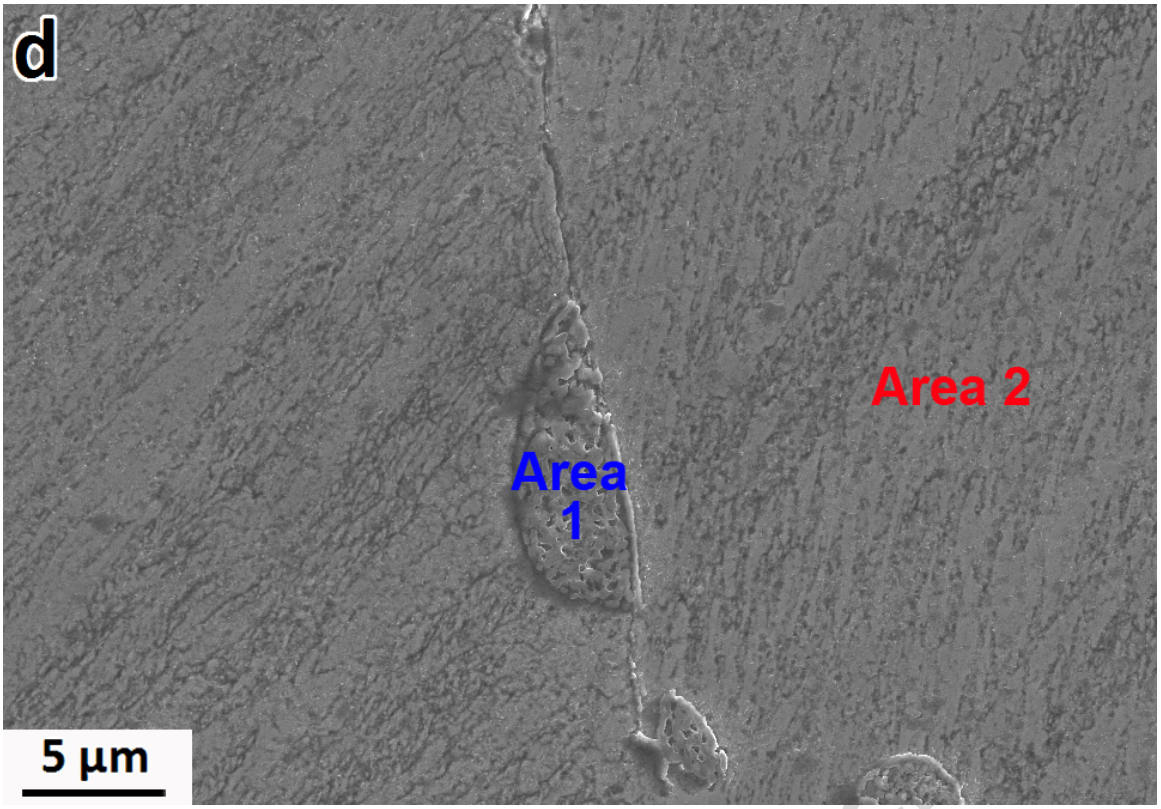

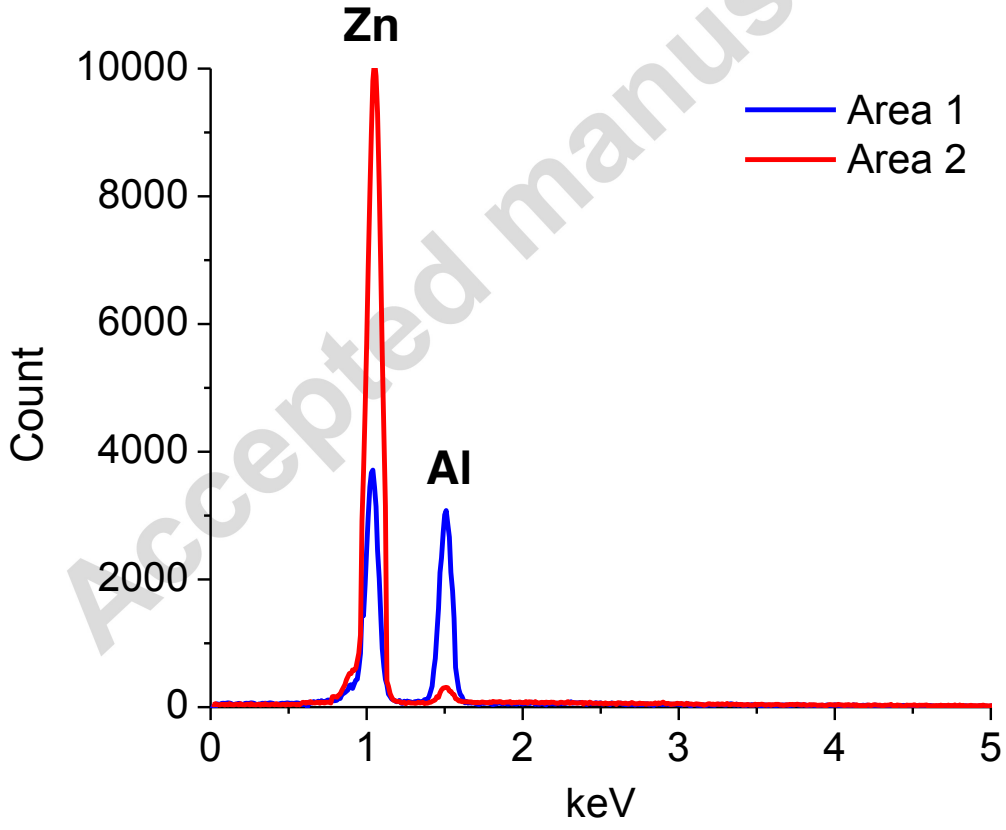

Fig. 2. SEM micrographs of the thermal treated Zn-1Al alloy after (a and c) 24 and (b and d) 48 hours and their corresponding EDS spectra on the given areas.

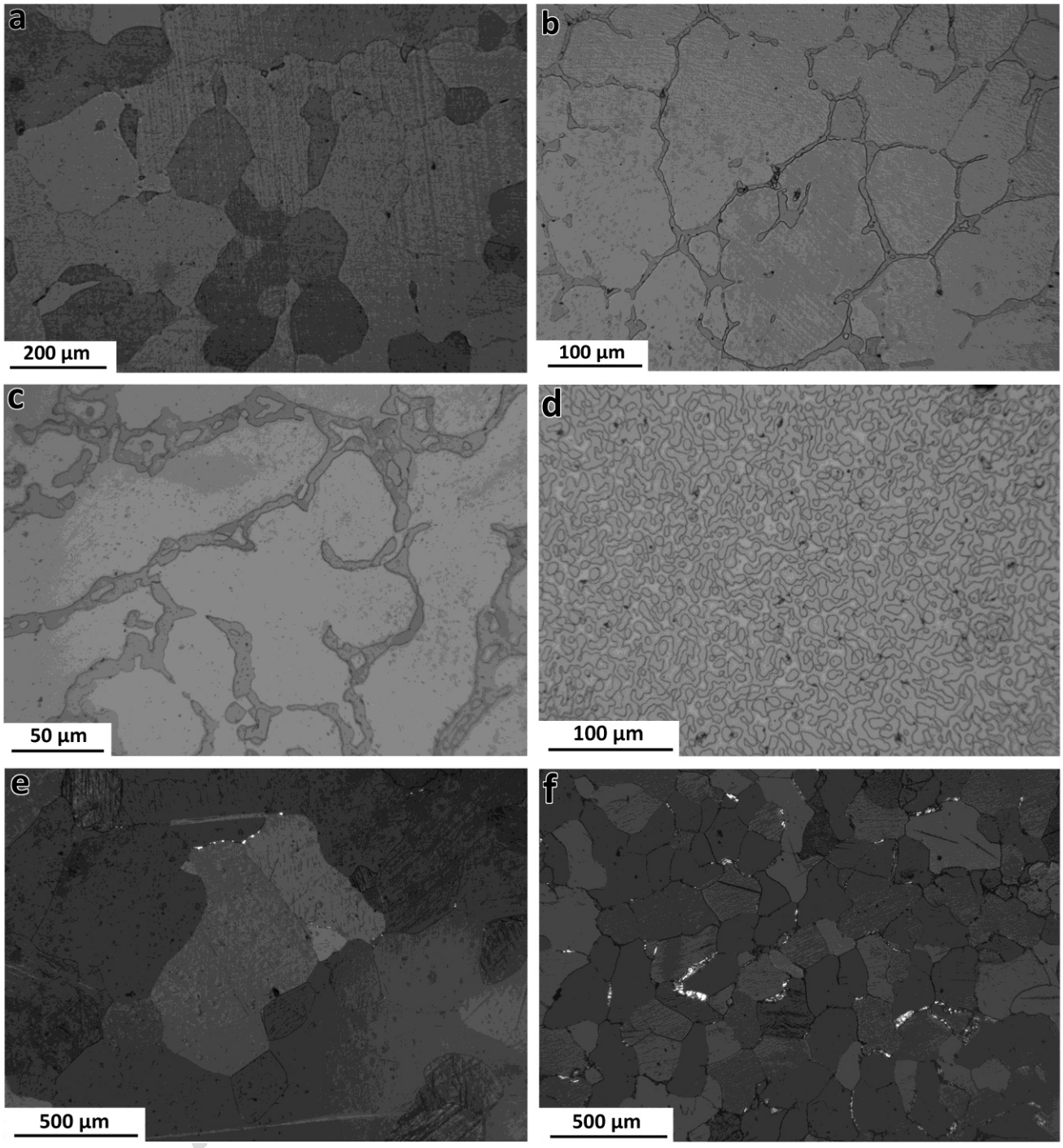

Fig. 3. Microstructure of the thermal treated samples: (a) Zn, (b) Zn-0.15Mg, (c) Zn-0.5Mg, (d) Zn-1Mg, (e) Zn-3Mg (f) Zn-0.5Al and (g) Zn-1Al.

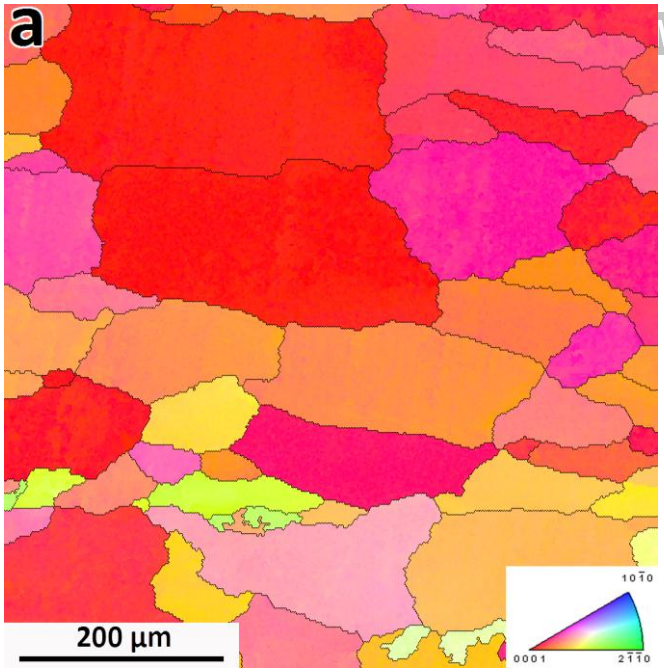

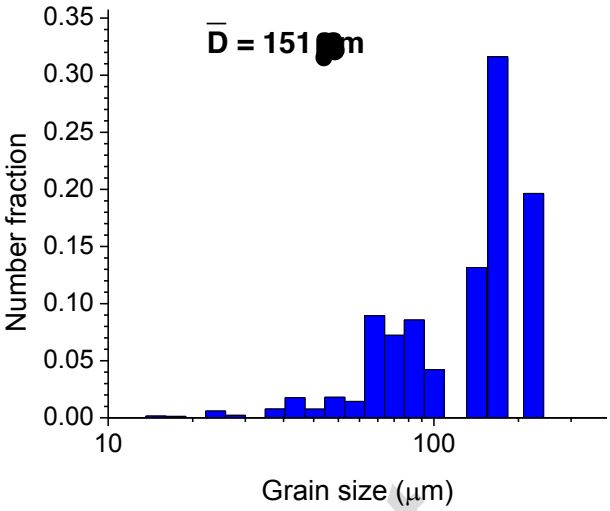

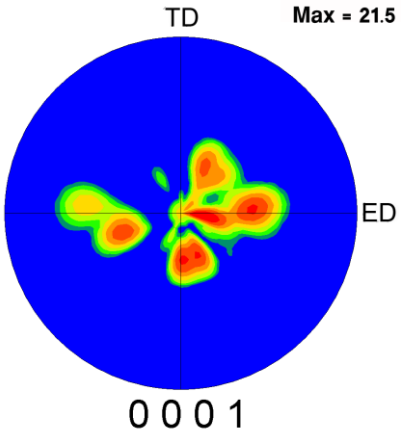

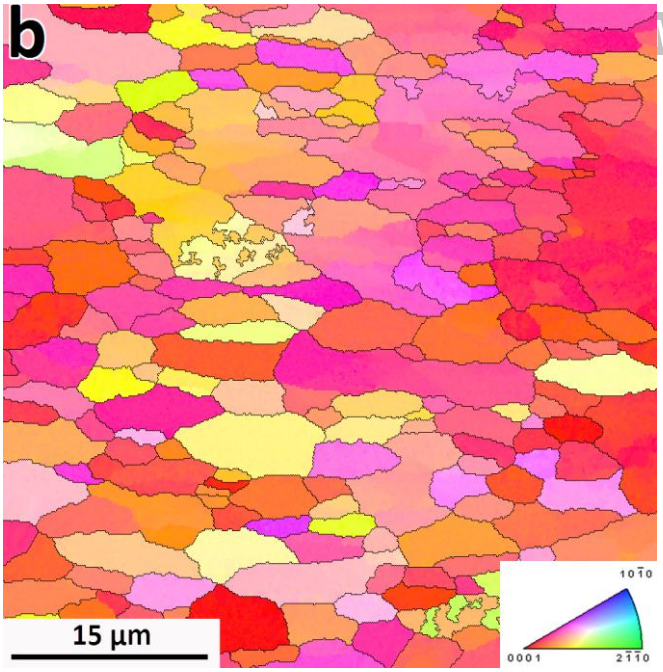

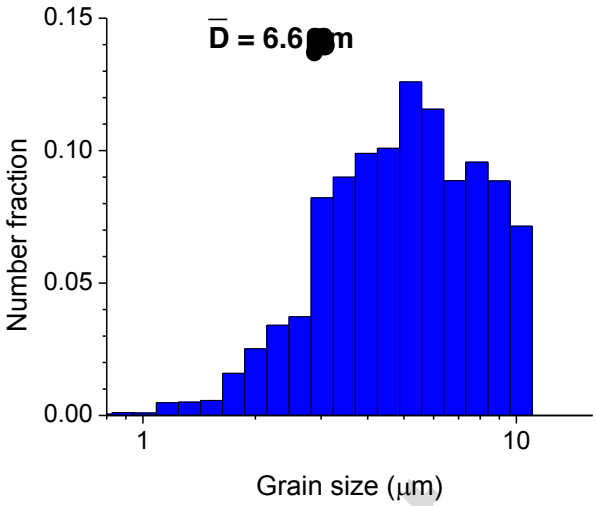

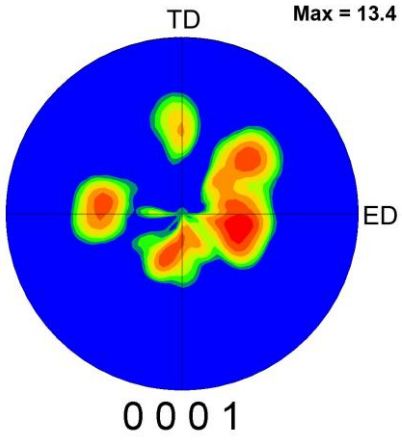

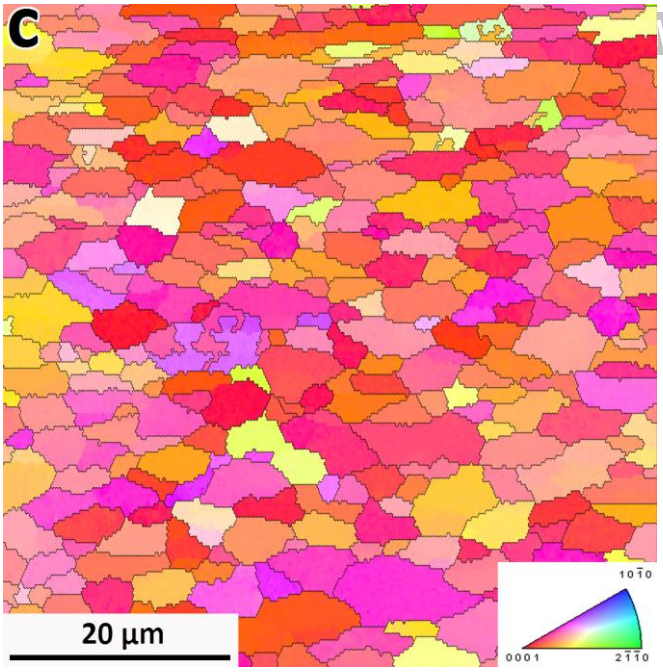

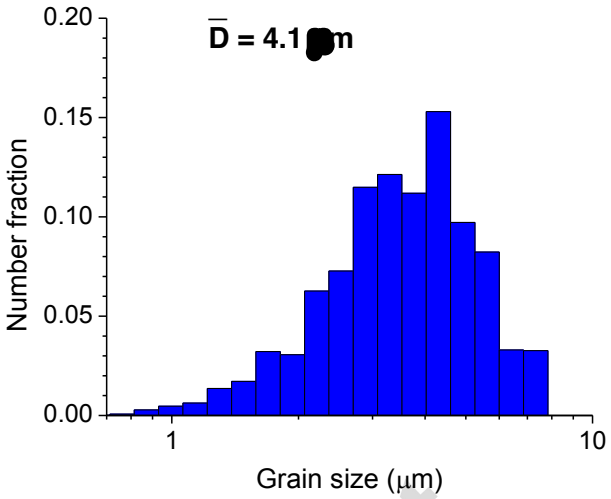

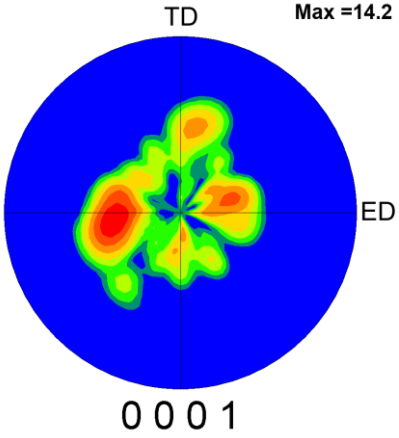

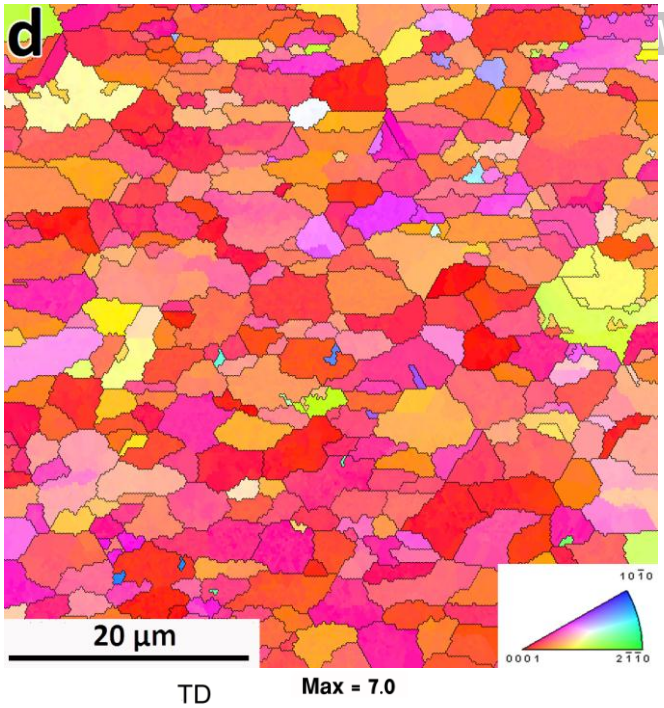

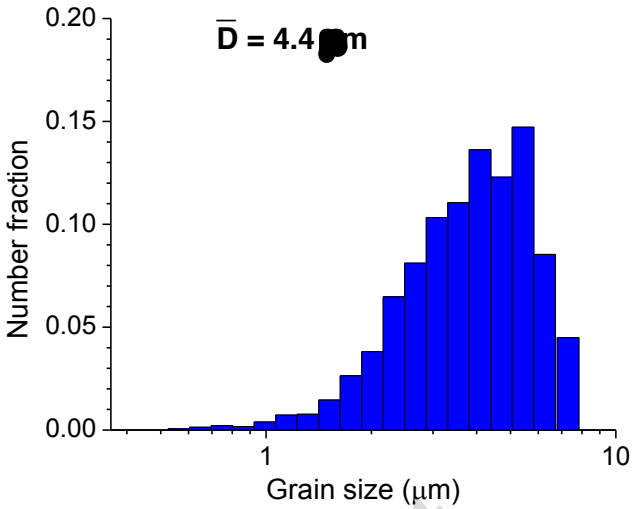

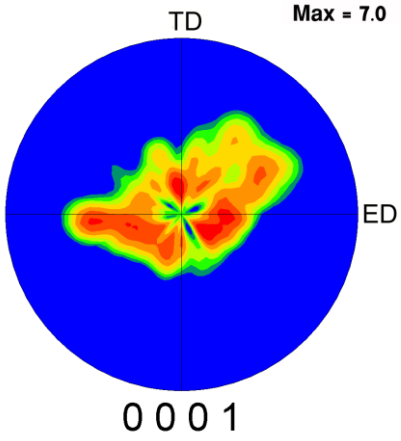

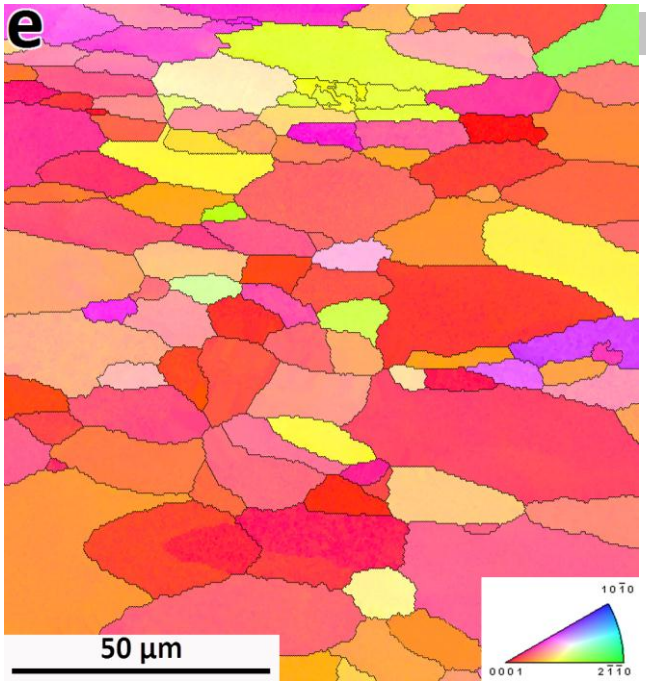

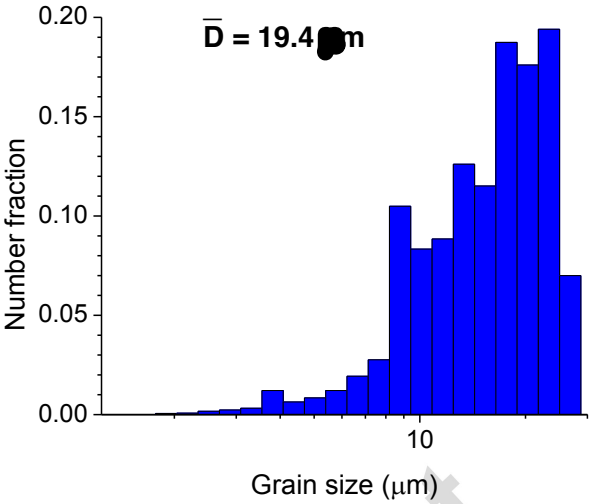

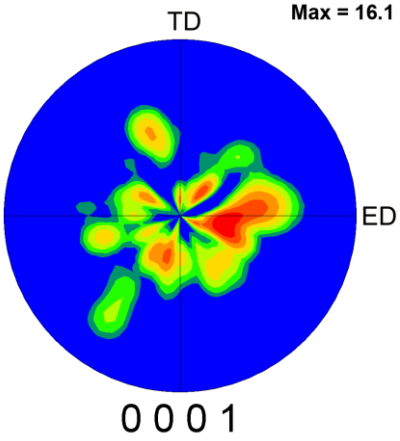

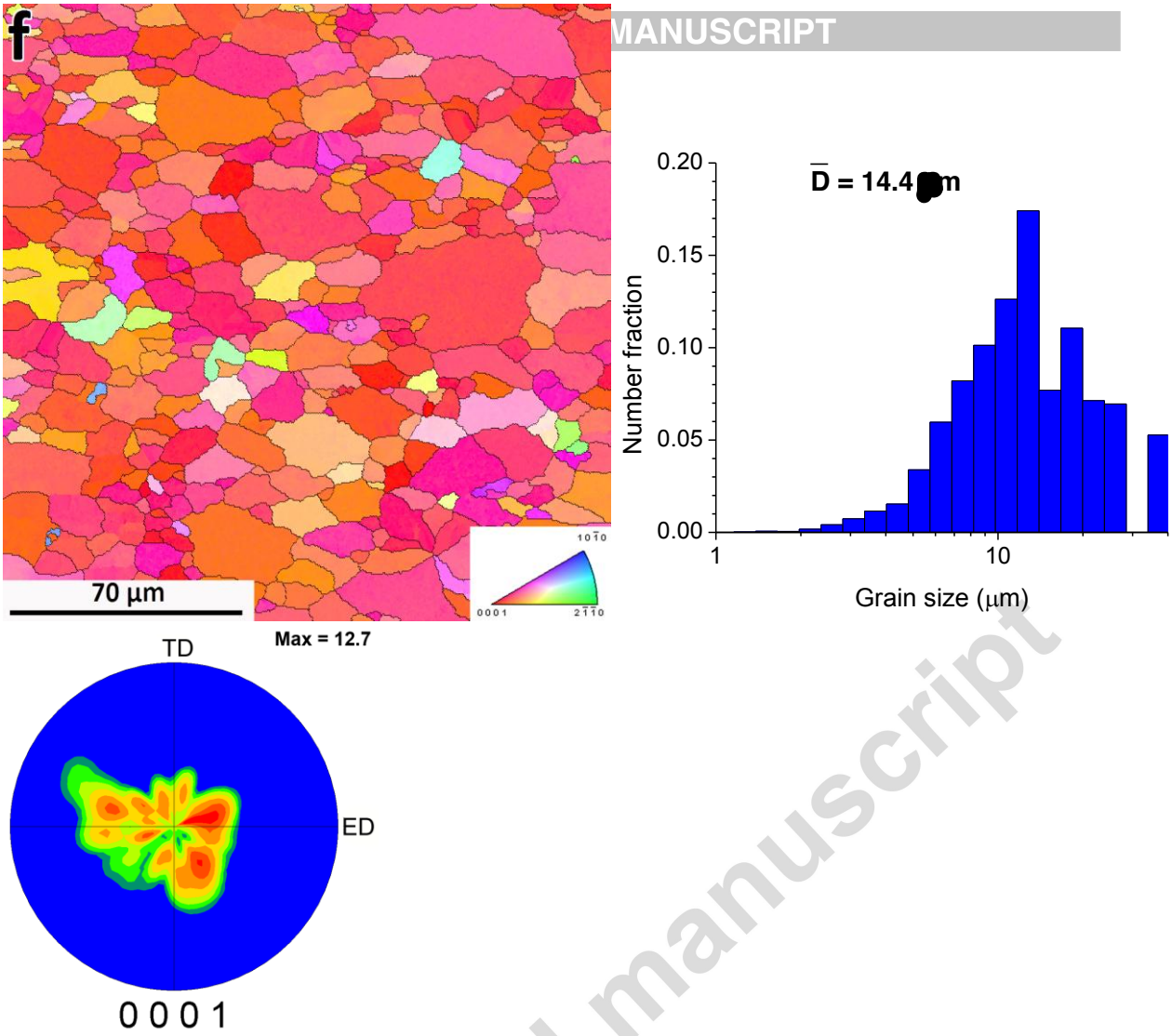

Fig. 4. EBSD orientation map, grain size distribution and (0001) pole figure of (a) Zn, (b) Zn-0.15Mg, (c) Zn-0.5Mg, (d) Zn-1Mg, (e) Zn-0.5Al and (f) Zn-1Al extruded samples. The color code of orientation maps is given by the reference triangle in the bottom right corner.

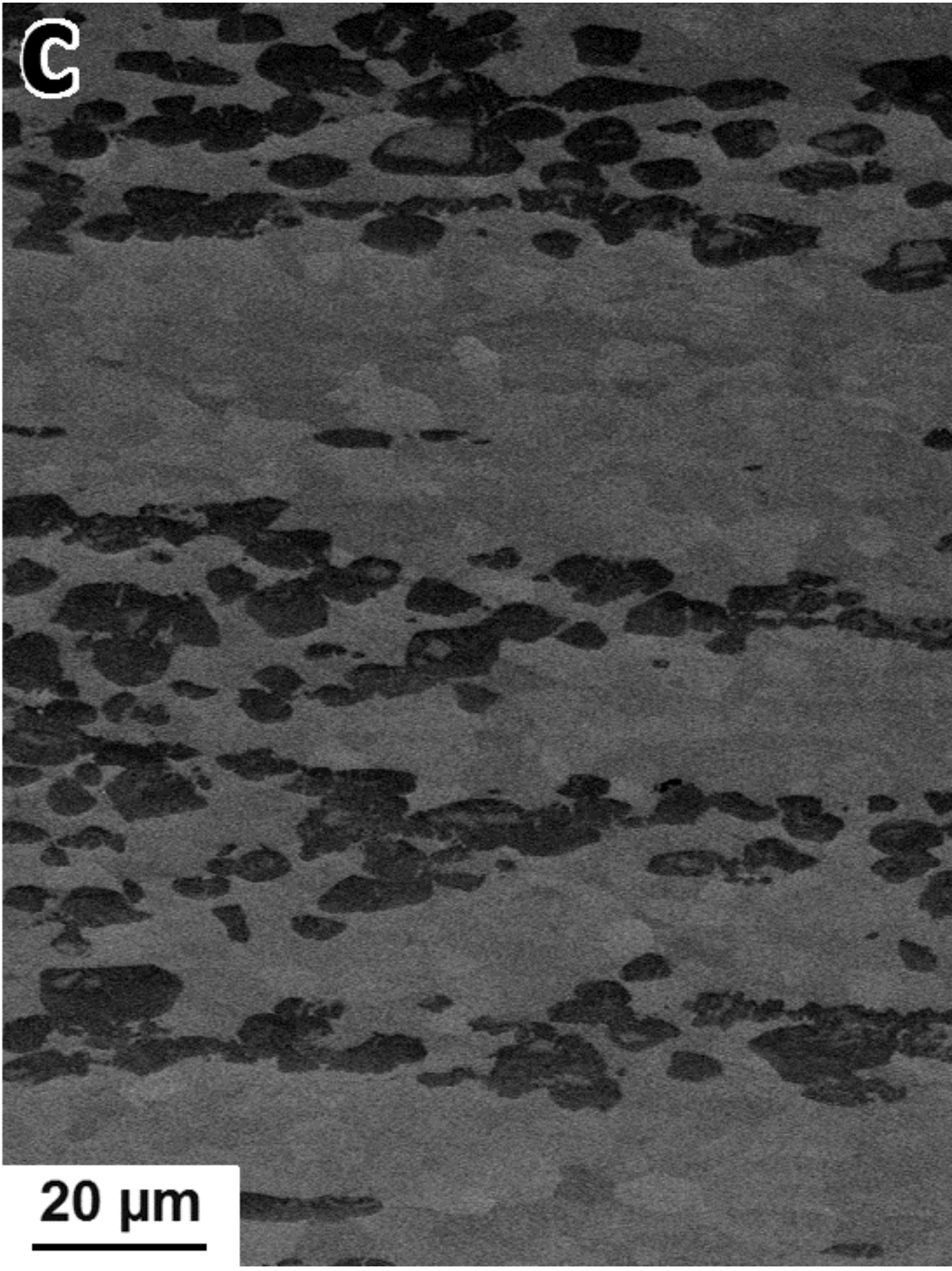
C
20 µm

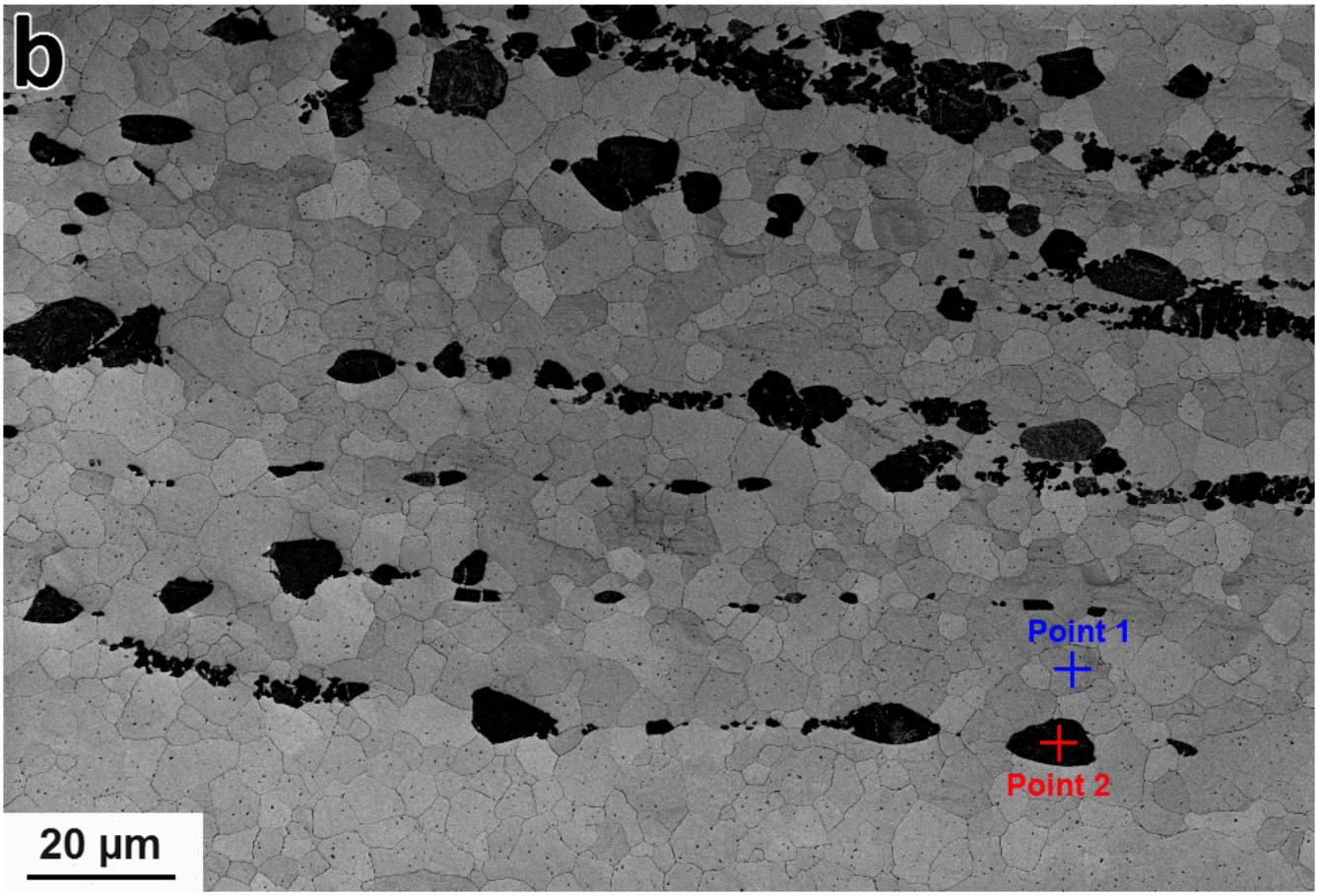

Count (a.u.)

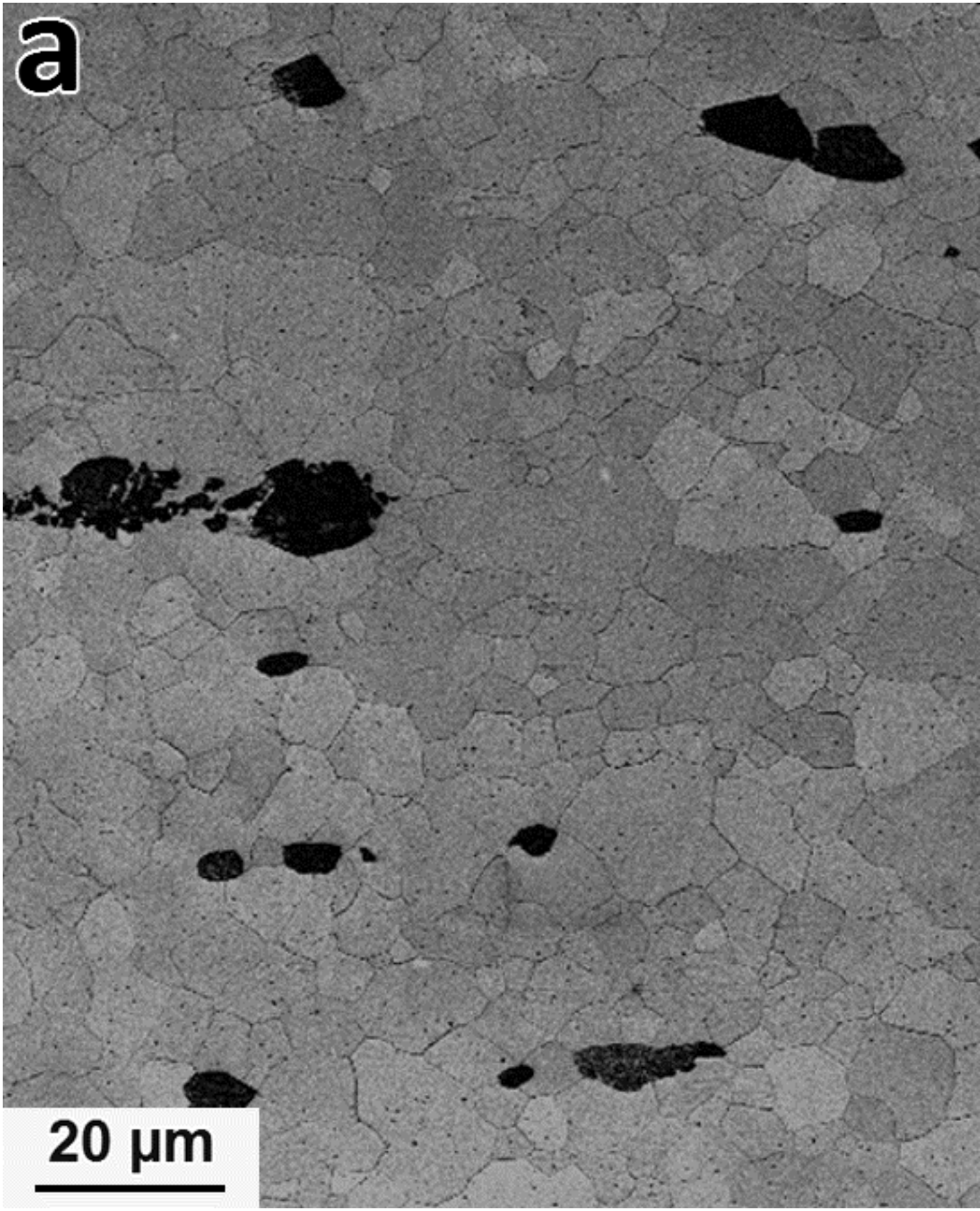
a
20 µm

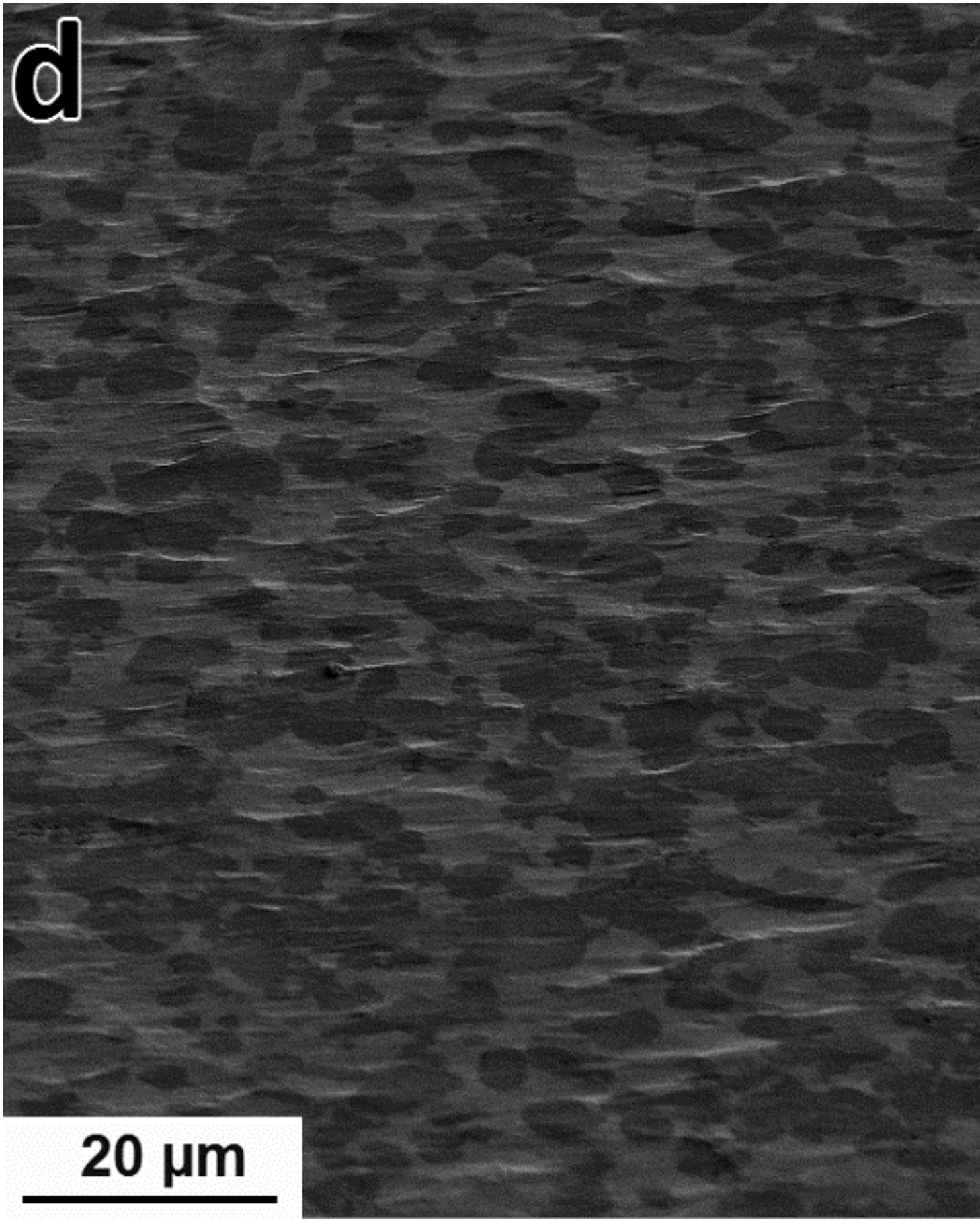
d
20 µm

Fig. 5. (a) SEM micrograph of Zn-0.5Mg alloy showing representative points A and B (b) EDS analysis of point A and B.


a
10 µm

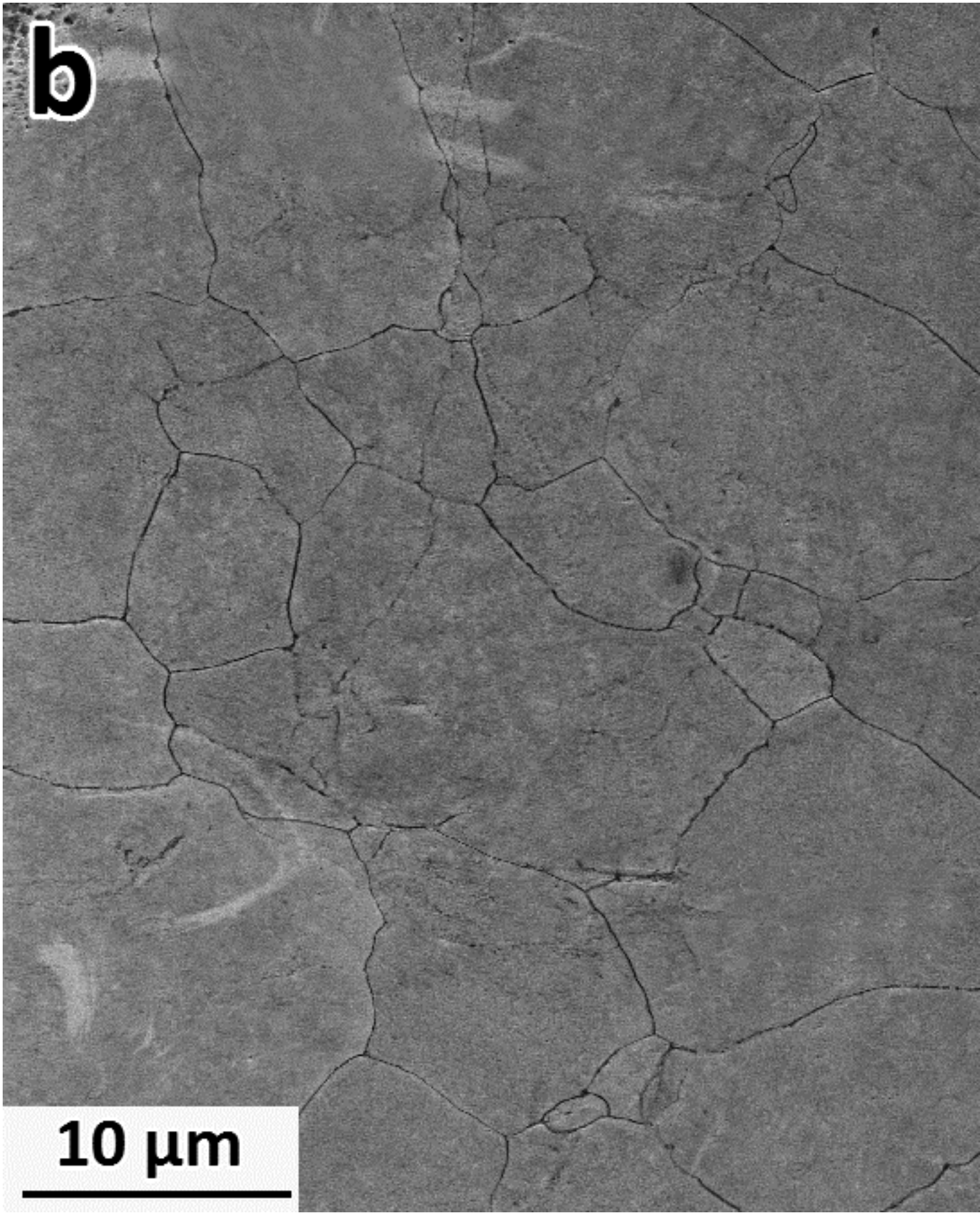

Fig. 6. (a) SEM micrographs of Zn-0.5Al, (b) Zn-1Al alloys.

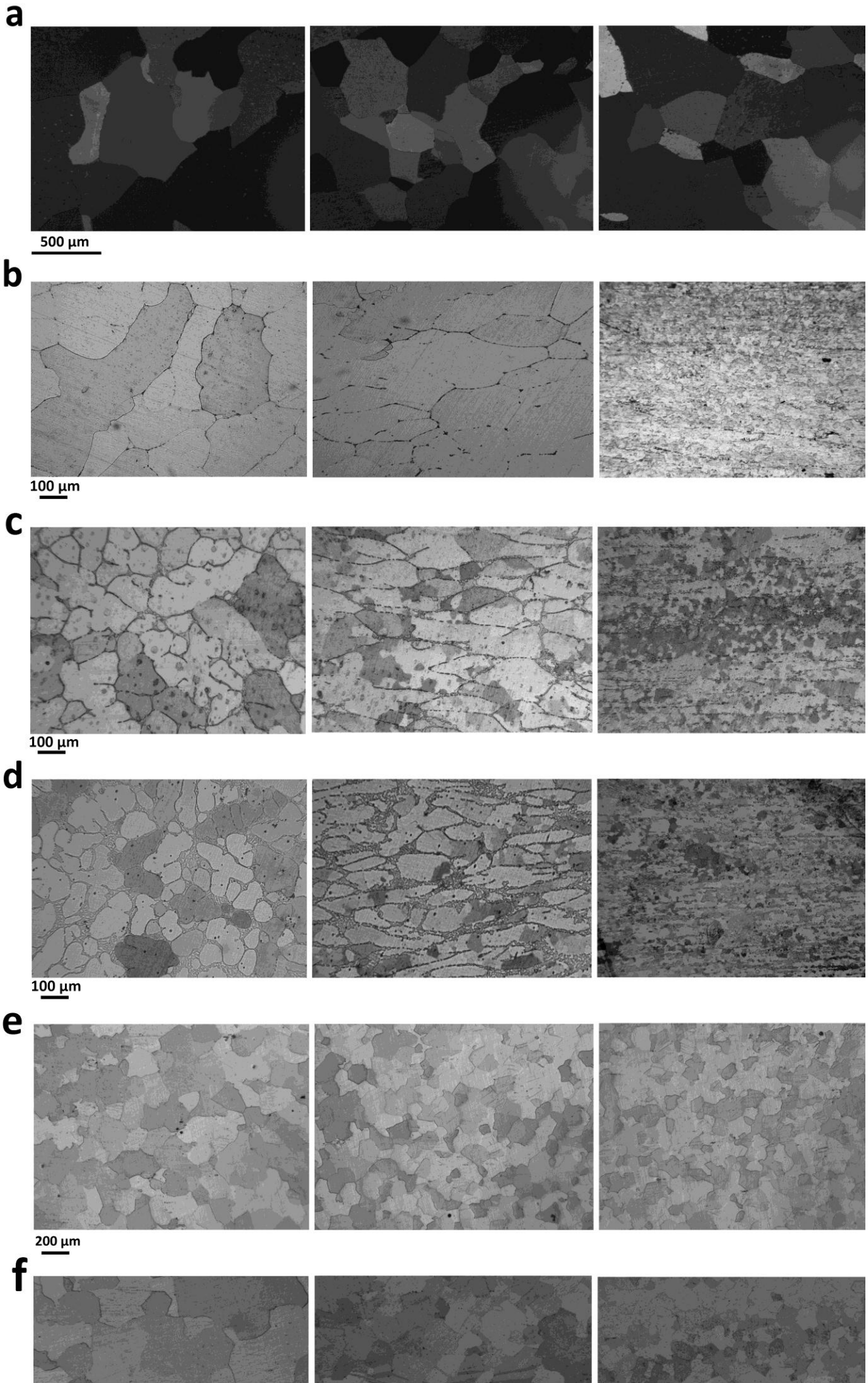
a
500 µm
b
100 µm
c
100 µm
d
100 µm
e
200 µm
f

Fig. 7. Microstructural evolution of the samples from interrupted tube extrusion trials. Left; undeformed billet; center; moderate and increasing deformation; right; in the extruded tube, high deformation. (a) Zn, (b) Zn-0.15Mg, (c) Zn-0.5Mg, (d) Zn-1Mg, (e) Zn-0.5Al and (f) Zn-1Al.

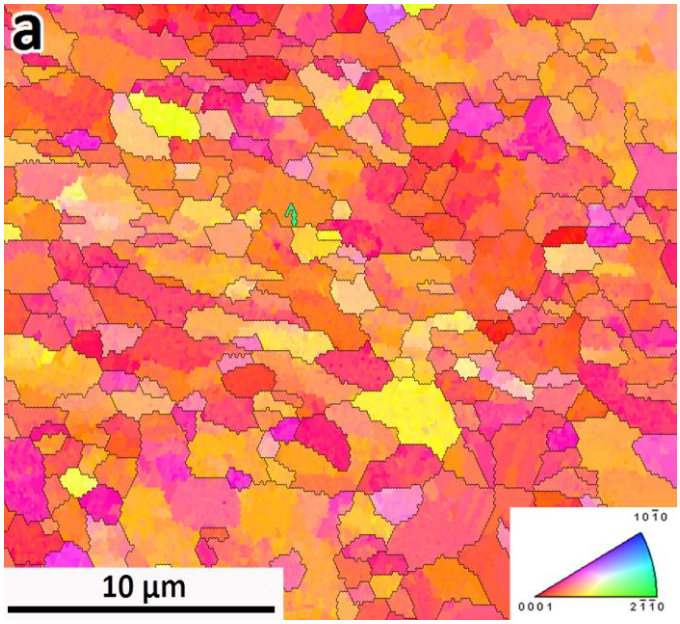

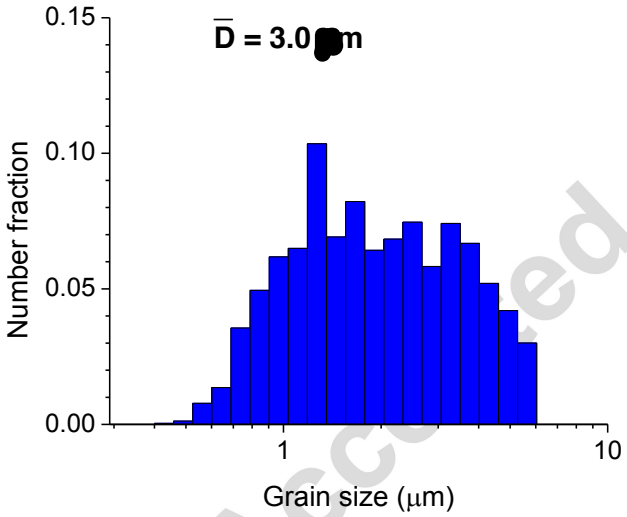

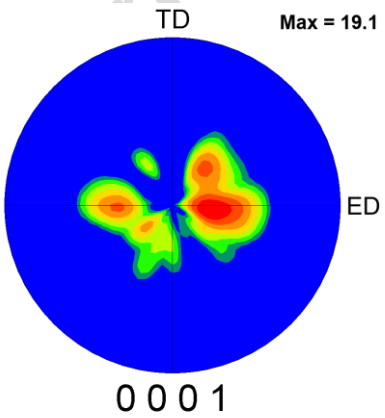

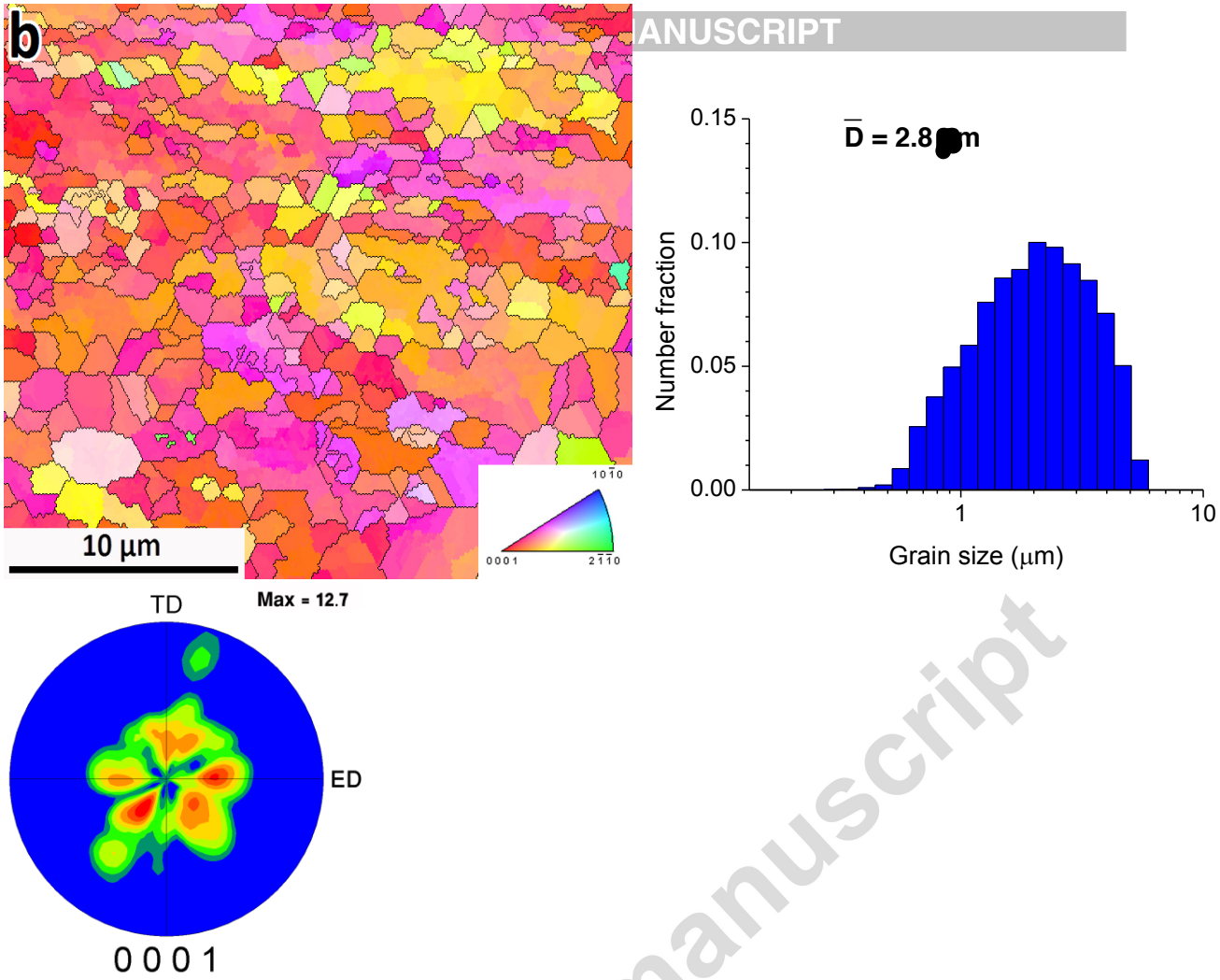

Fig. 8. EBSD orientation map, grain size distribution and (0001) pole figure of (a) Zn-0.5Mg and (b) Zn-1Mg extruded tubes.

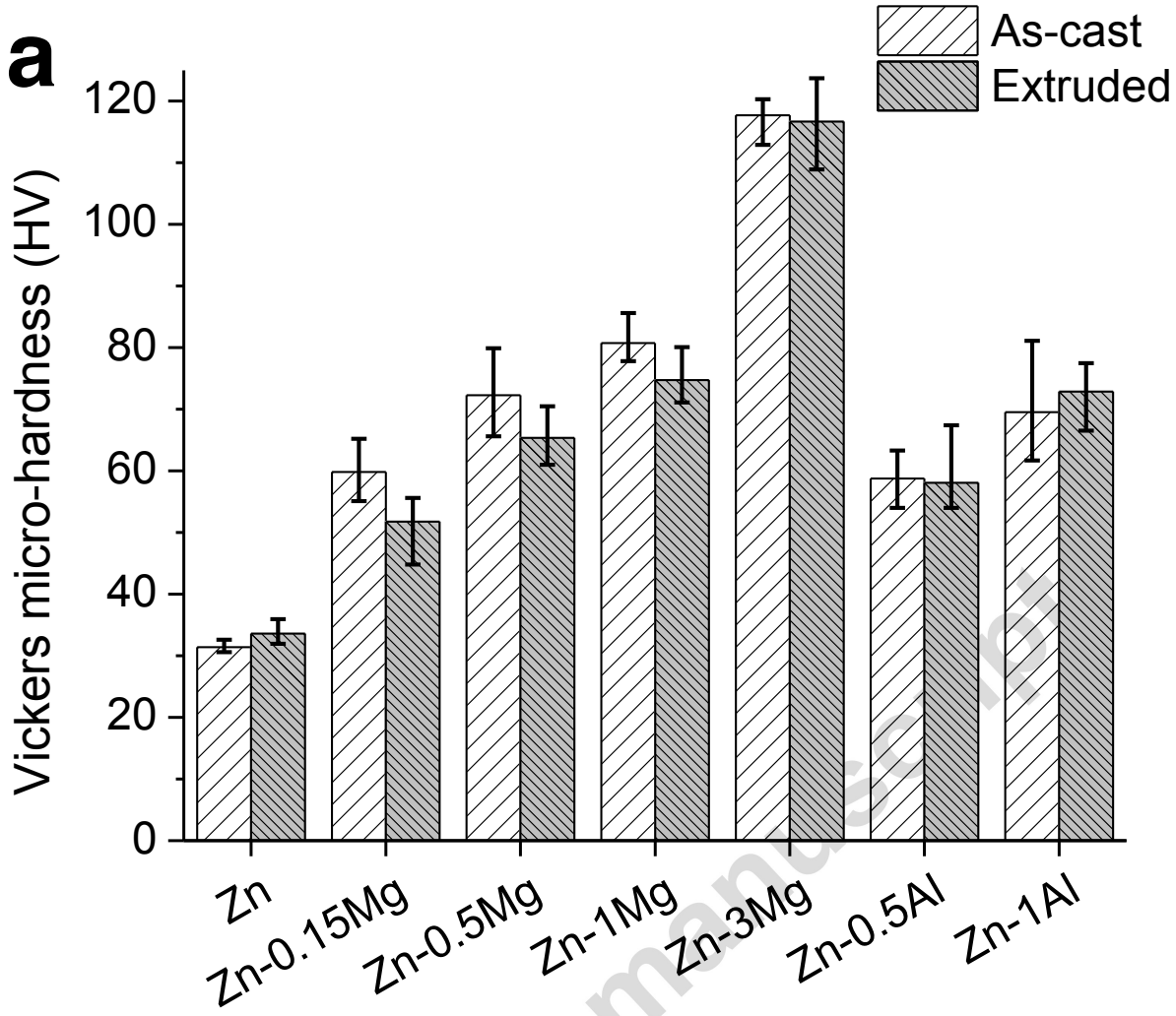

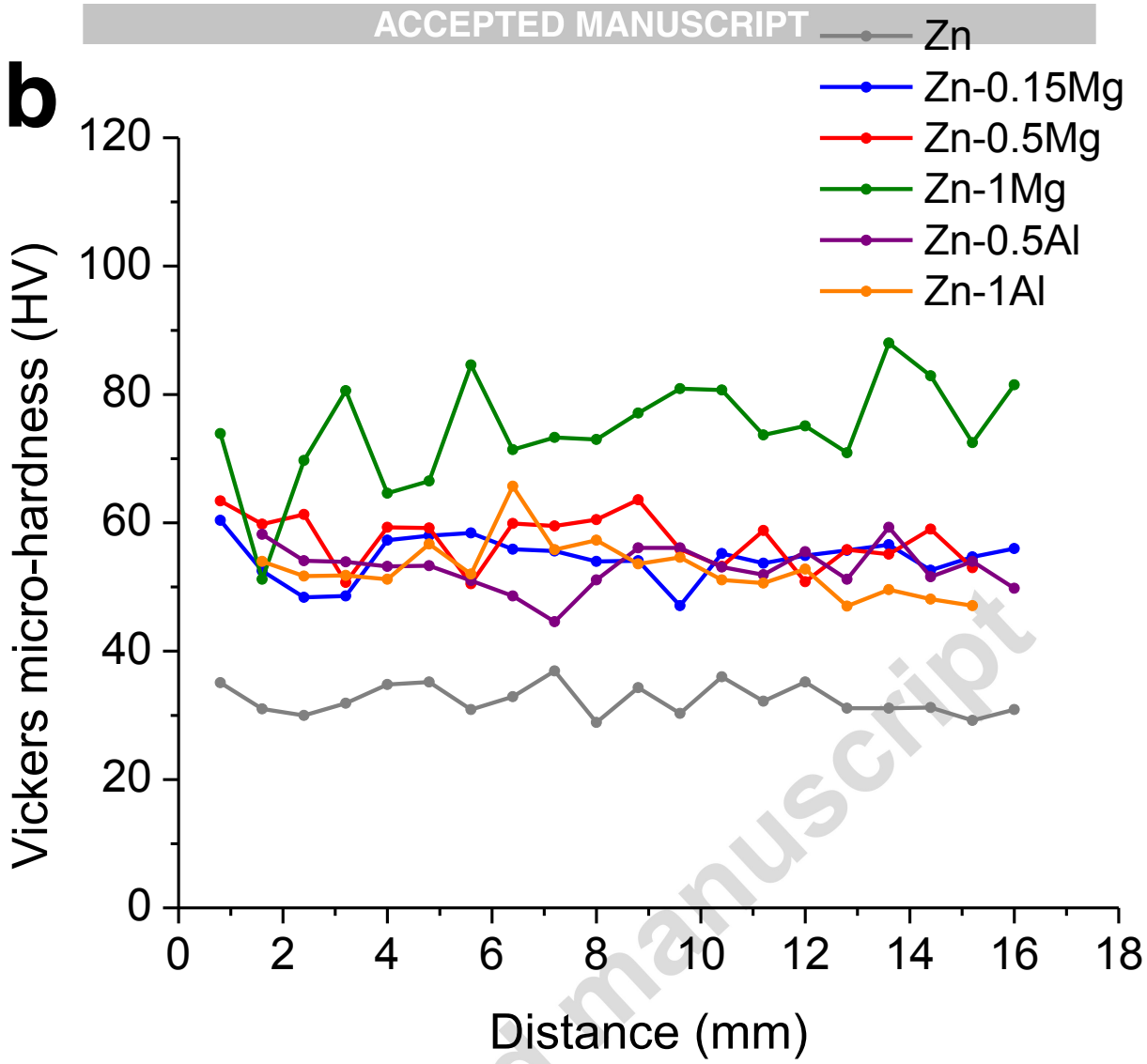

Fig. 9. Comparison of micro-hardness of the cast and extruded samples (a) and micro-hardness profiles on longitudinal cross sections of the samples subjected to interrupted extrusion tests (b).

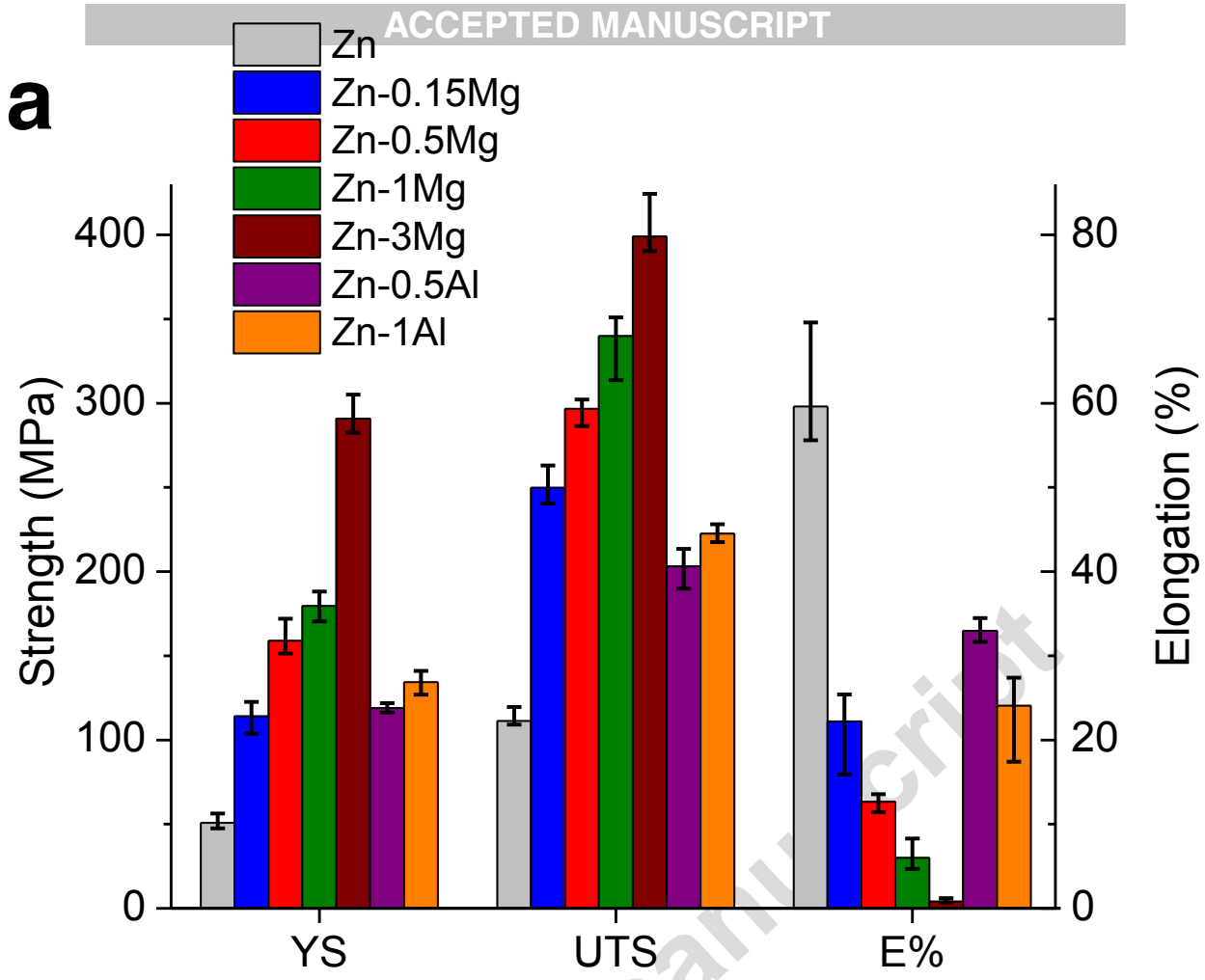

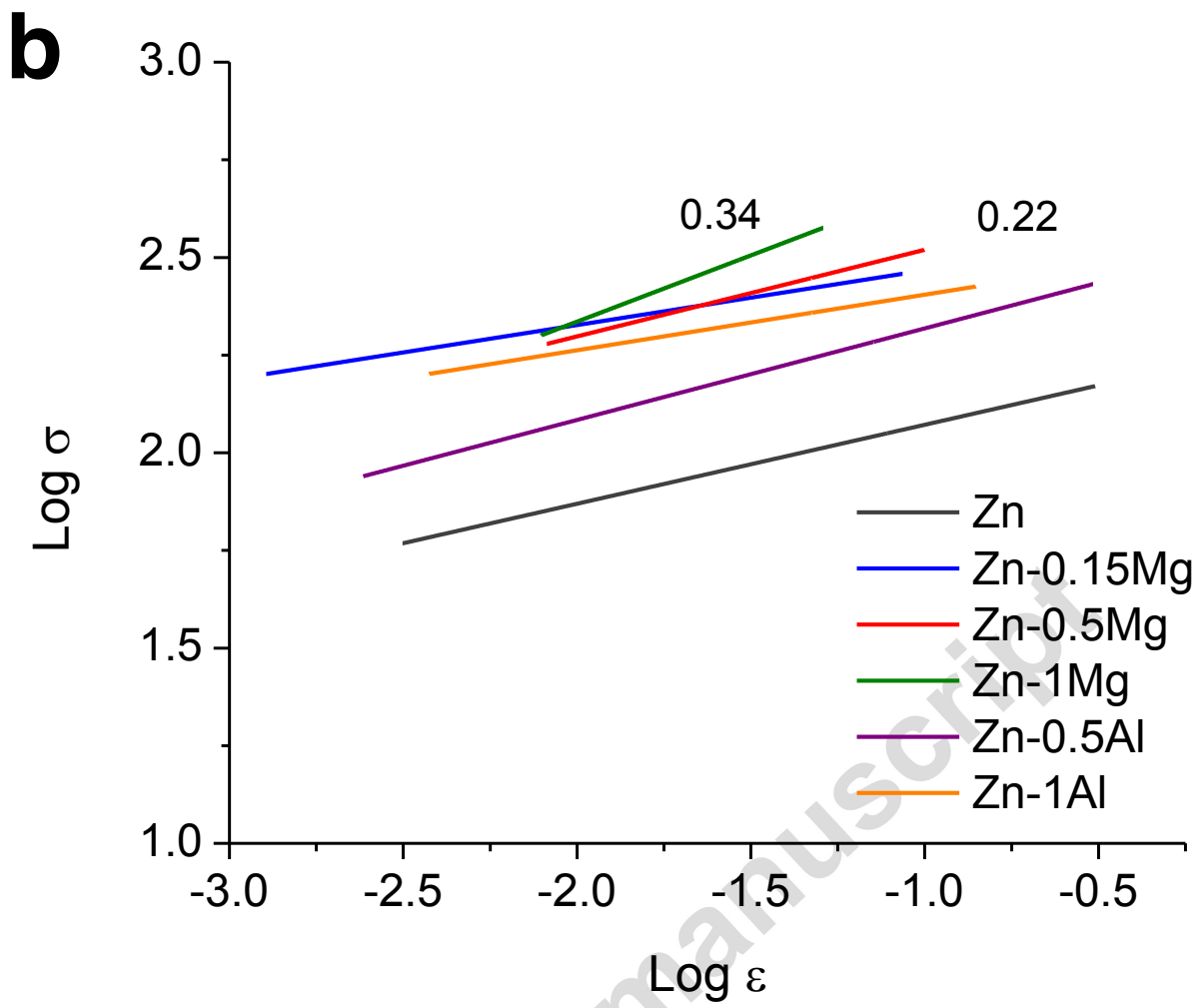

Fig. 10. (a) Tensile properties and (b) work hardening exponents calculated from the tensile curves for all samples.

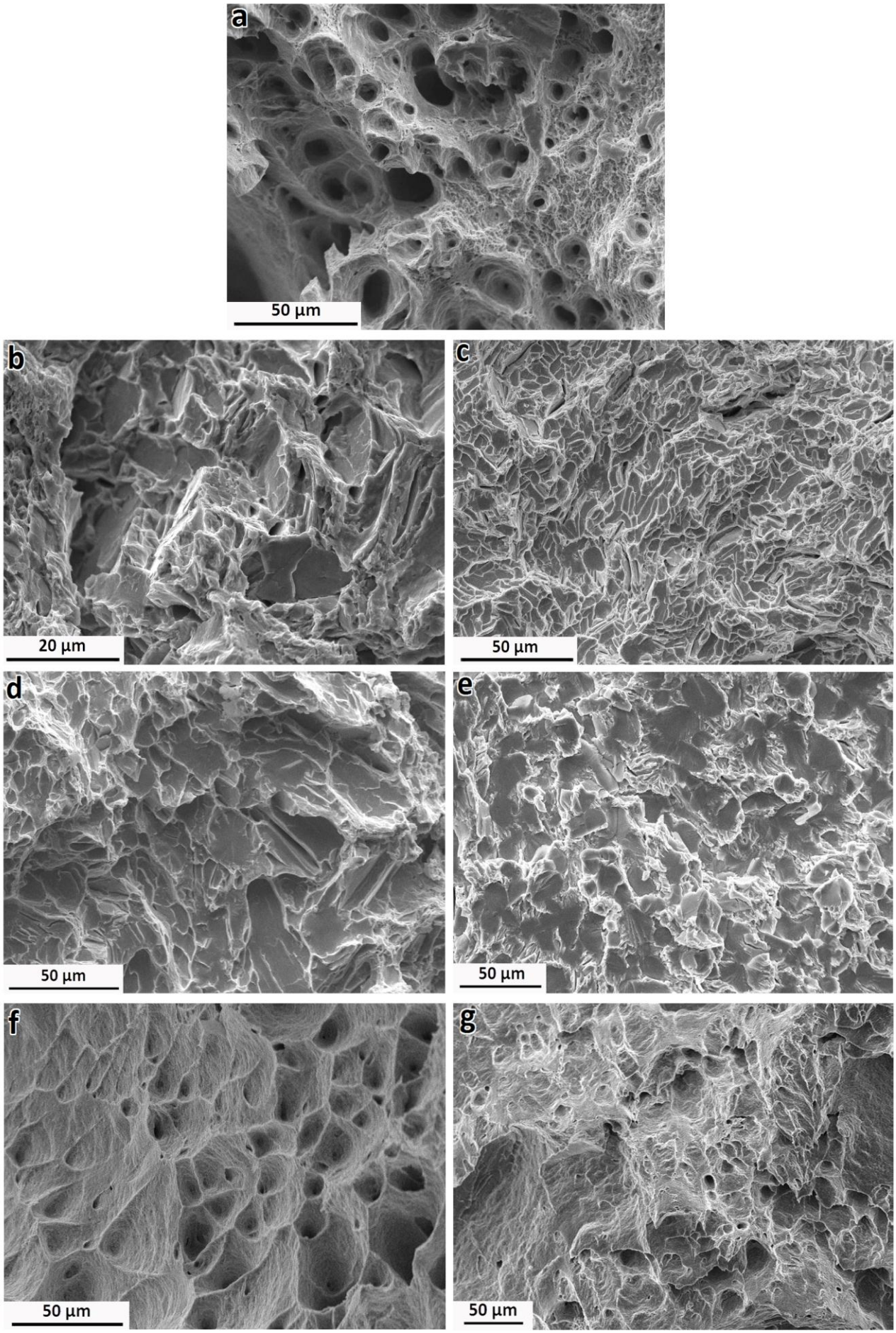
a
50 µm
b
20 µm
c
50 µm
d
50 µm
e
50 µm
f
50 µm
g
50 µm

Fig. 11. SEM morphology of the tensile fracture surface of the extruded pure Zn and Zn-based alloy samples: (a) pure Zn, (b) Zn–0.15Mg, (c) Zn–0.5Mg, (d) Zn–1Mg, (e) Zn-3Mg, (f) Zn-0.5Al and (g) Zn-1Al.

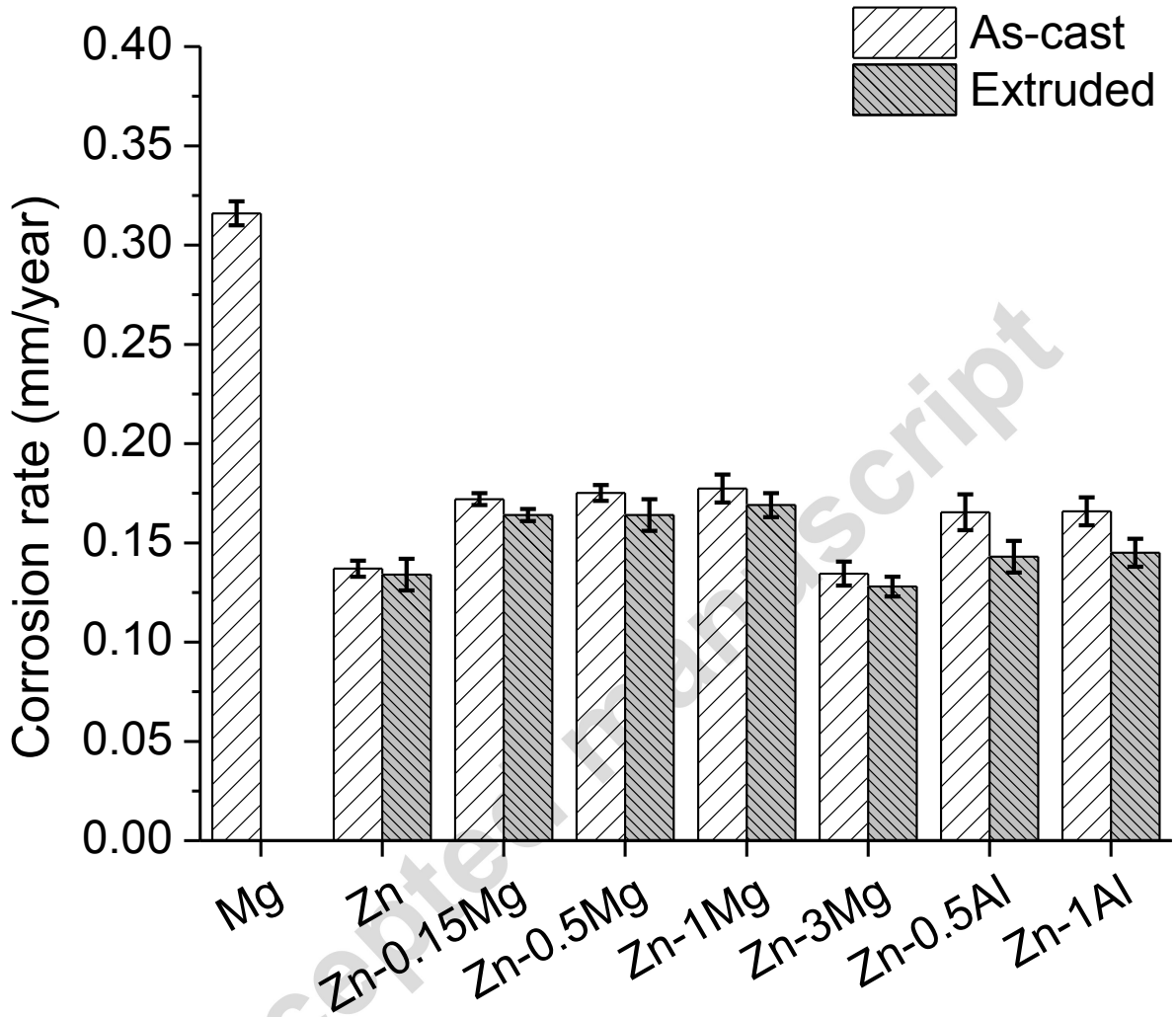

Fig. 12. Corrosion rates of as-cast and extruded alloys with Zn and Mg as controls.

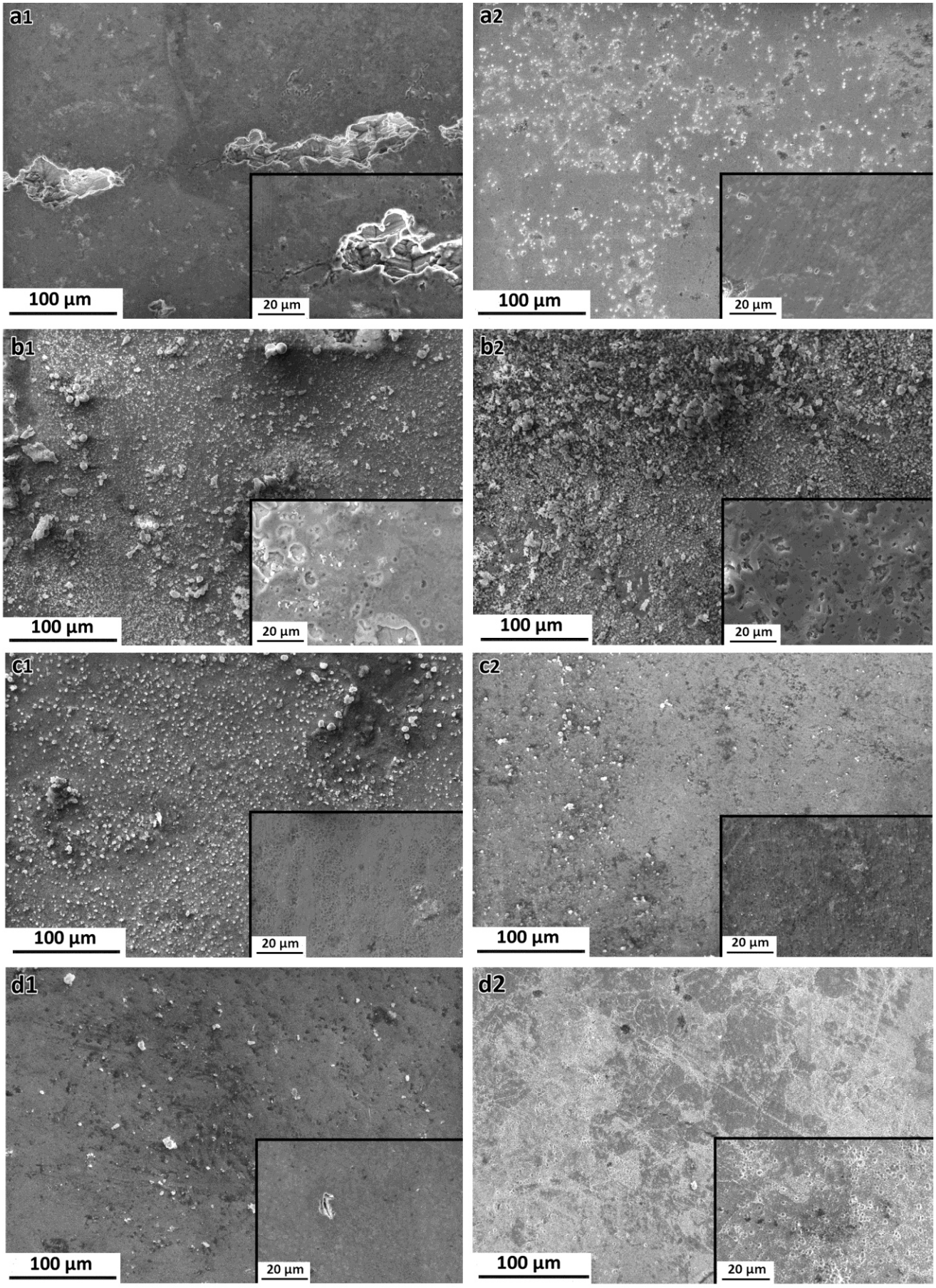
a1
100 µm
20 µm
a2
100 µm
20 µm
b1
100 µm
20 µm
b2
100 µm
20 µm
c1
100 µm
20 µm
c2
100 µm
20 µm
d1
100 µm
20 µm
d2
100 µm
20 µm

Fig. 13. SEM images showing the surface morphologies of as cast and extruded alloys after electrochemical tests. a1) Zn-I, a2) Zn-E, b1) Zn-0.15Mg as-cast, b2) Zn-0.15Mg extruded, c1) Zn-3Mg as-cast, c2) Zn-3Mg extruded d1) Zn-1Al as-cast d2) Zn-1Al extruded.

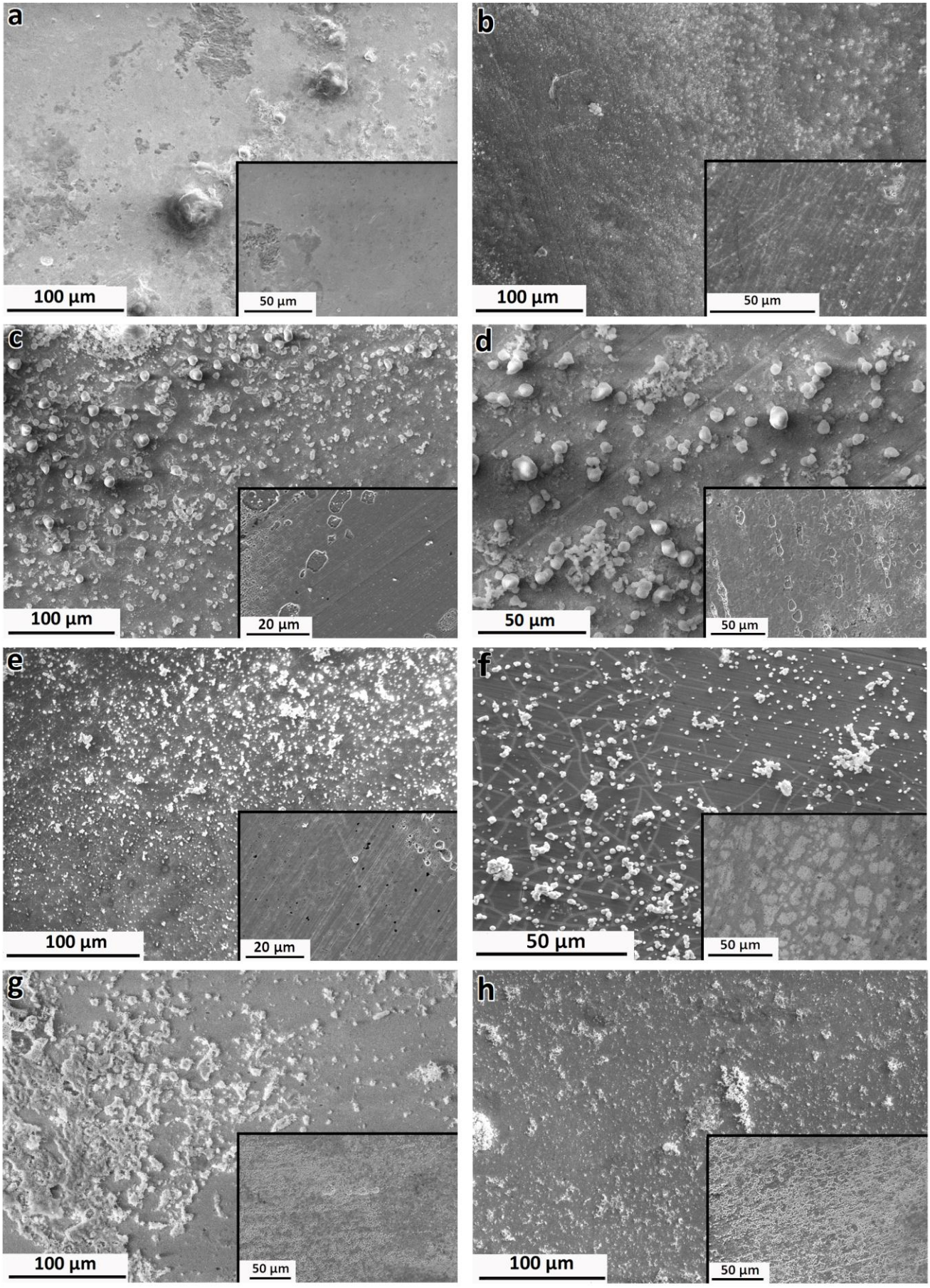
a
100 µm
50 µm
b
100 µm
50 µm
c
100 µm
20 µm
d
50 µm
50 µm
e
100 µm
20 µm
f
50 µm
50 µm
g
100 µm
50 µm
h
100 µm
50 µm

Fig. 14. SEM images showing the surface morphologies of Zn and Zn binary alloys after 336 hours immersion in modified Hanks' solution, before and after removal of corrosion products: a) Zn-I, b) Zn-E, c) Zn-0.15Mg, d) Zn-0.5Mg, e) Zn-1Mg, f) Zn-3Mg, g) Zn-0.5Al, h) Zn-1Al.

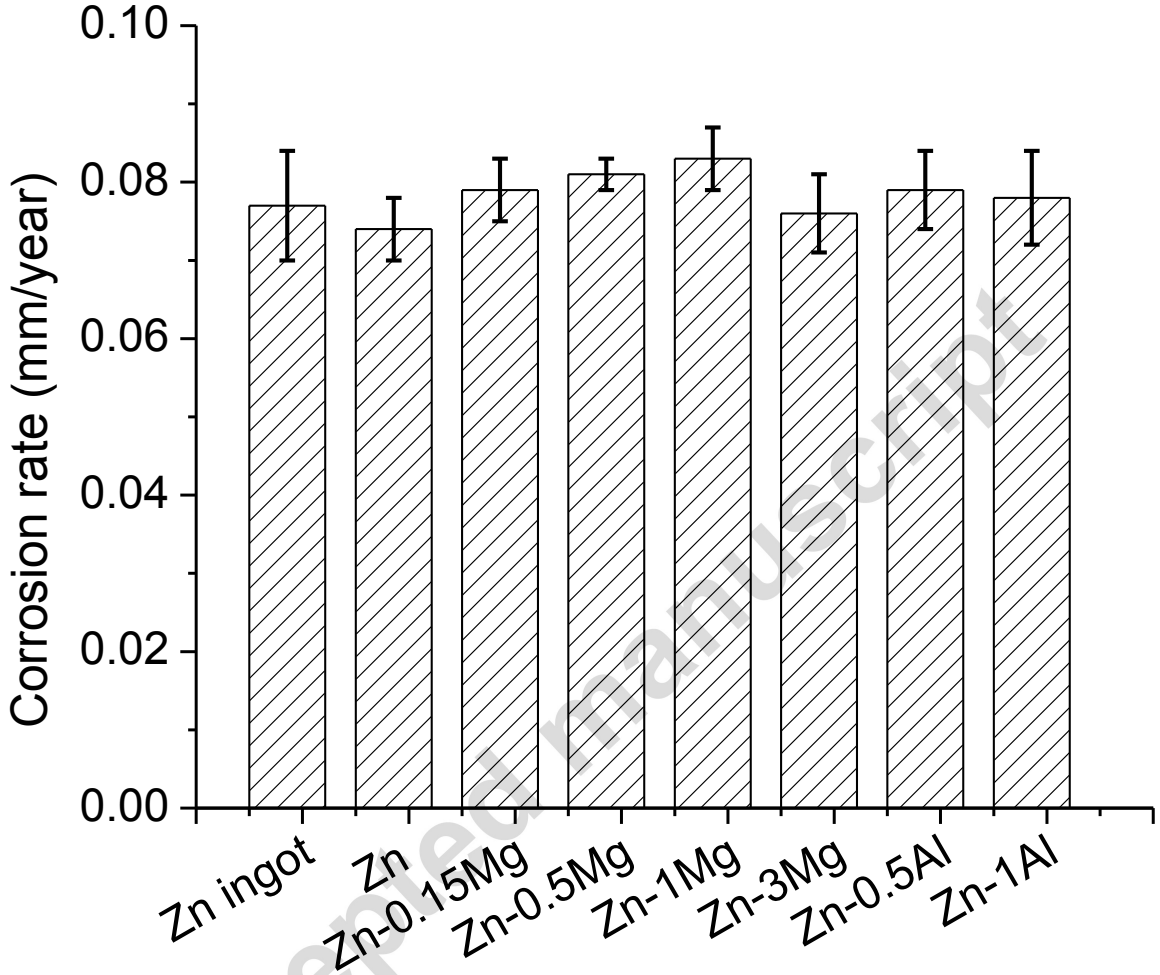

Fig. 15. Corrosion rates of extruded alloys with a Zn control, calculated on the base of weight loss tests.

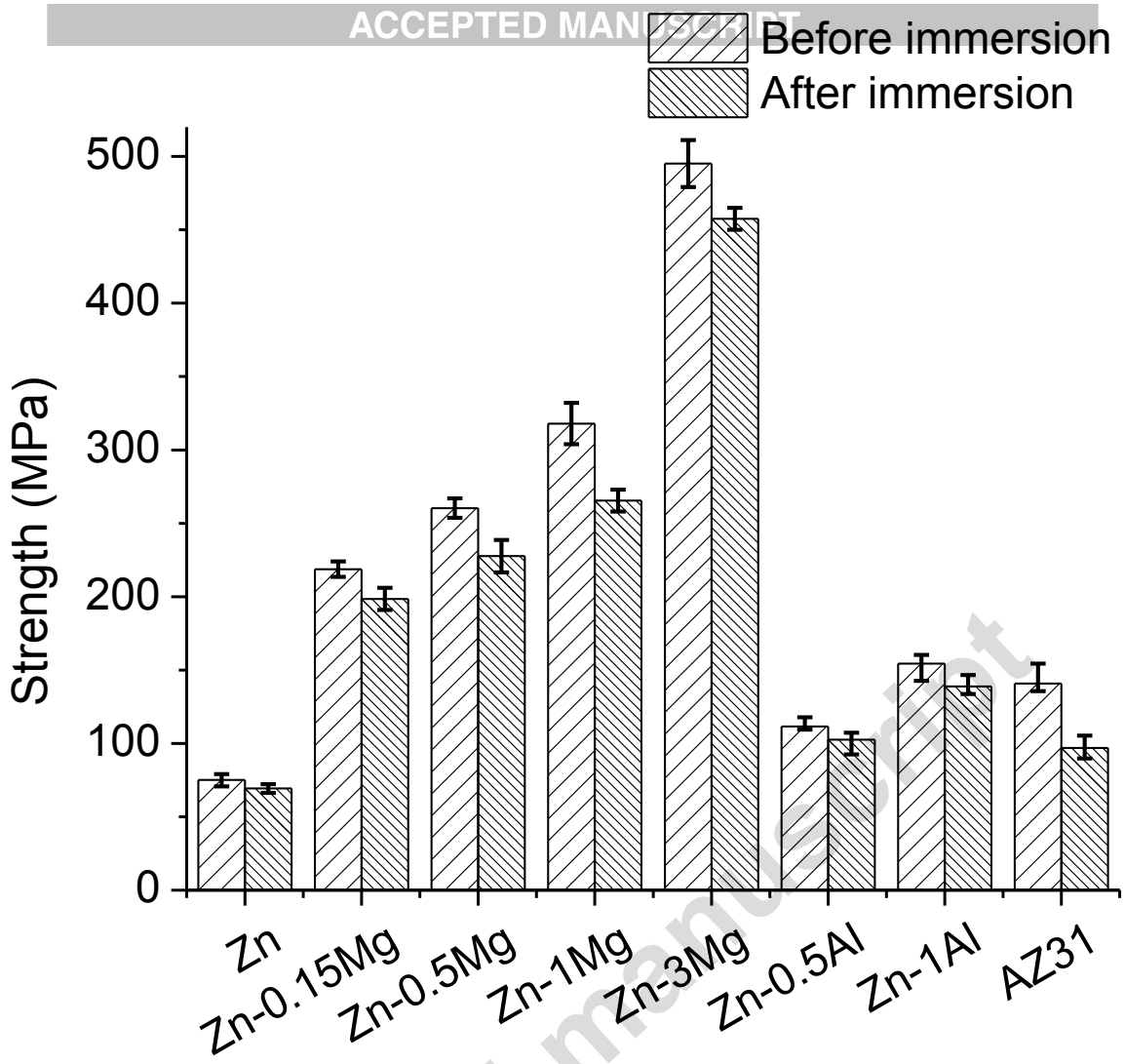

Fig. 16. Compressive yield strength values of the samples at room temperature before and after immersion in Hanks' modified solution.

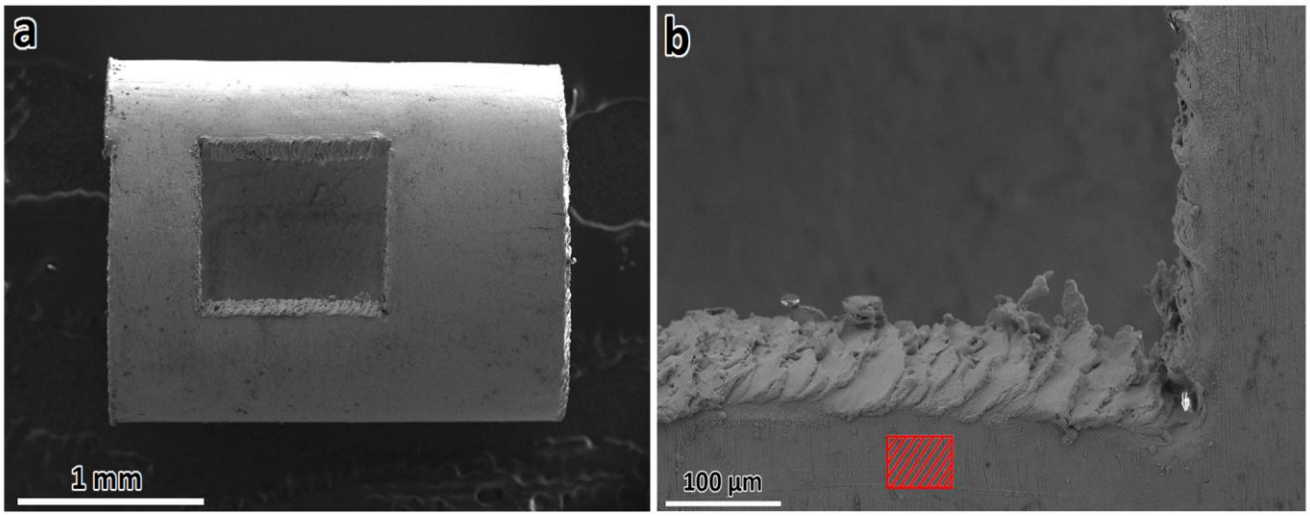

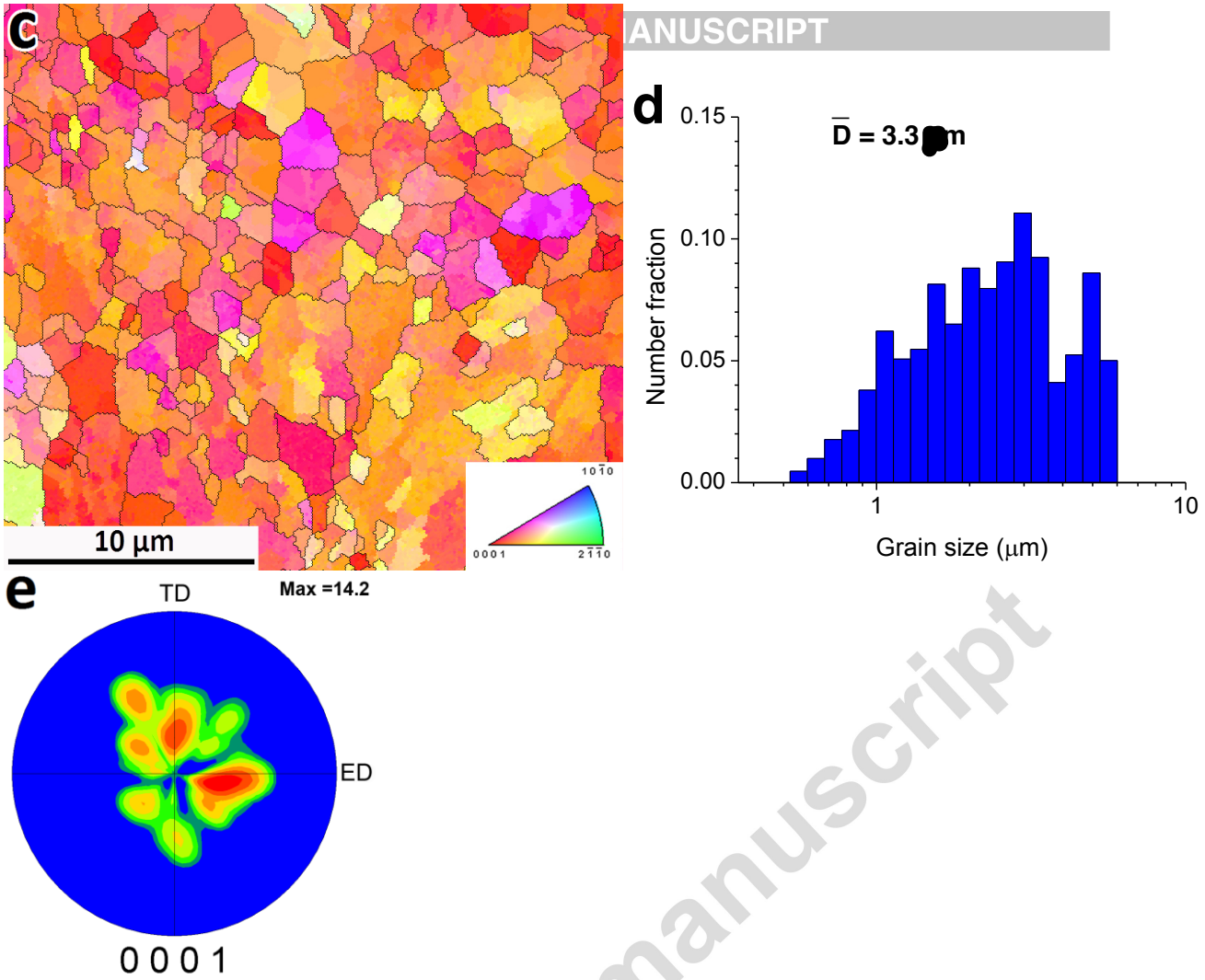

Fig. 17. (a) SEM view of the laser processed Zn-0.5Mg mini-tube (b) magnified view near the edge of cut pocket, (c) EBSD orientation map next to the laser cut edge and (d) its corresponding grain size distribution and (e) (0001) pole figure.

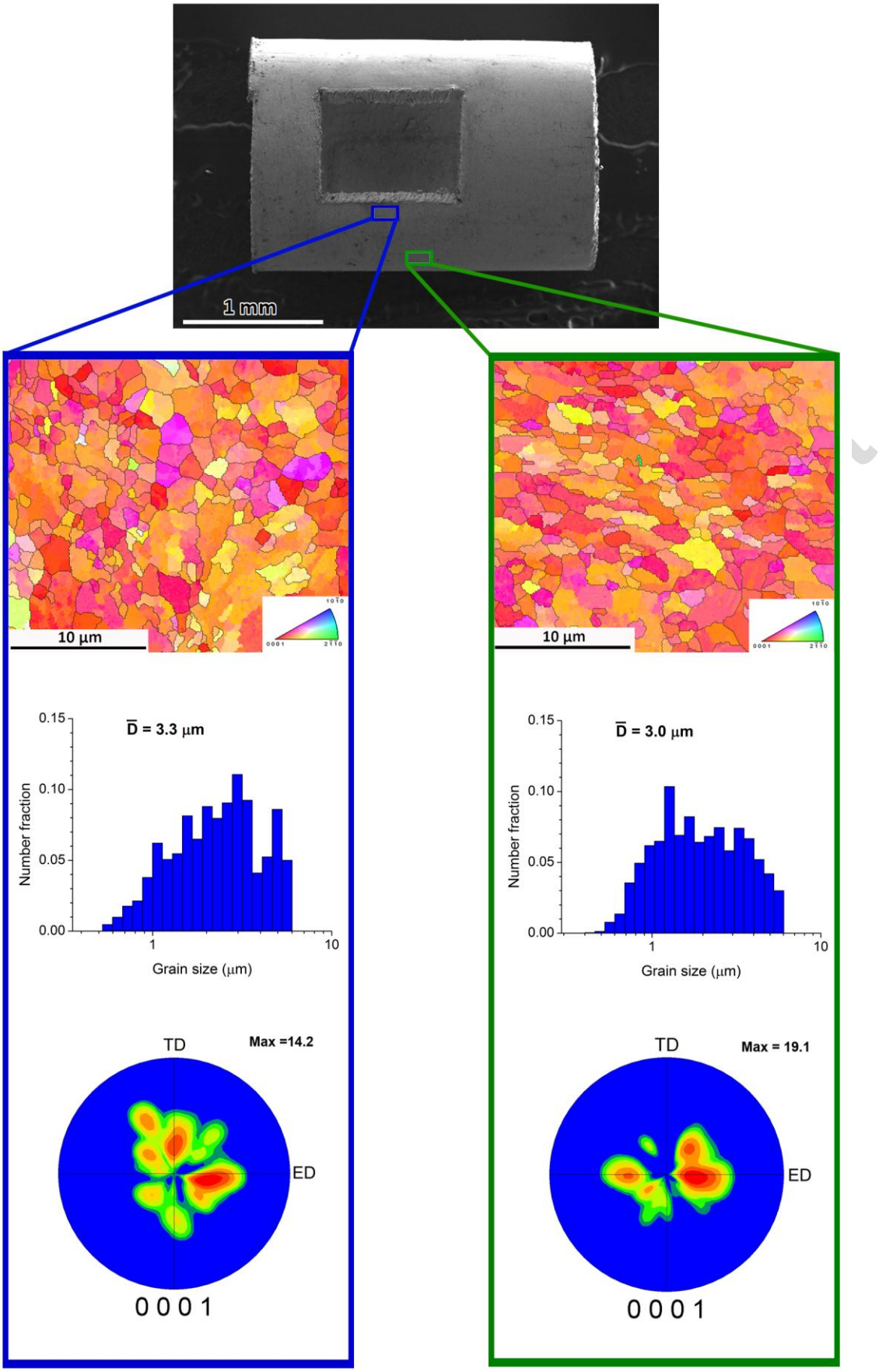

Tables

Table 1. Nominal composition of the investigated samples.

Sample	Zn (wt%)	Mg (wt.%)	Al (wt.%)
Pure Zn	100	-	-
Zn-0.15Mg	99.85	0.15	-
Zn-0.5Mg	99.5	0.5	-
Zn-1Mg	99	1	-
Zn-3Mg	97	3	-
Zn-0.5Al	99.5	-	0.5
Zn-1Al	99	-	1

Table 2. Mechanical properties and average grain size of the investigated extruded billets.

Sample	Grain size (μm)	YS (MPa)	UTS (MPa)	E (%)	Micro-hardness (HV)
Zn	151 ± 19.6	51 ± 3.7	111 ± 4.5	60 ± 5.9	34 ± 1.7
Zn-0.15Mg	6.6 ± 0.8	114 ± 7.7	250 ± 9.2	22 ± 4.0	52 ± 4.9
Zn-0.5Mg	4.1 ± 0.4	159 ± 8.5	297 ± 6.5	13 ± 0.9	65 ± 3.9
Zn-1Mg	4.4 ± 0.5	180 ± 7.3	340 ± 15.6	6 ± 1.1	75 ± 3.9
Zn-3Mg	-	291 ± 9.3	399 ± 14.4	1 ± 0.1	117 ± 6.1
Zn-0.5Al	19.4 ± 2.8	119 ± 2.3	203 ± 9.6	33 ± 1.2	59 ± 5.8
Zn-1Al	14.4 ± 1.2	134 ± 5.8	223 ± 4.3	24 ± 4.2	73 ± 4.6

Table 3. Corrosion parameters of as-cast and extruded alloys determined from the potentiodynamic measurements.

Sample	Condition	E_c (V)	j (μA/cm^2)
Mg	Ingot	-1.56	17.16
Zn	Ingot	-0.99	9.20
	Extruded	-0.98	8.98

Zn-0.15Mg	As-cast	-1.03	11.52
	Extruded	-1.01	10.98
Zn-0.5Mg	As-cast	-1.05	11.73
	Extruded	-1.02	11.01
Zn-1Mg	As-cast	-1.07	11.88
	Extruded	-1.05	11.32
Zn-3Mg	As-cast	-0.98	9.01
	Extruded	-0.92	8.60
Zn-0.5Al	As-cast	-0.99	11.08
	Extruded	-0.98	9.60
Zn-1Al	As-cast	-0.99	11.11
	Extruded	-0.98	9.70

Table 4. Elemental composition of corrosion products of Zn and Zn-based alloys after immersion test in Hanks' modified solution.

Sample	Element (wt.%)								
	C	O	Na	Mg	Al	P	Cl	Ca	Zn
Zn	-	17	7.4	-	-	4.5	1.1	1.3	68
Zn-0.15Mg	3.6	26	5.3	0.4	-	6.3		1.5	56
Zn-0.5Mg	0.8	12	2.8	0.4	-	3.5	4.7	0.1	75
Zn-1Mg	2.4	17	3.6	0.4	-	5.7		1.5	69
Zn-3Mg	3.3	17	4.4	2.7	-	2.9	1.1	1.4	67
Zn-0.5Al	-	29	1.6	-	0.4	6.1	6.1	0.1	56
Zn-1Al	0.1	33	2.6	-	2.7	4.3	4.9	0.2	52

Table 5. Compressive yield strength reduction for the investigated samples after 336 hours of immersion.

Sample	Reduction in CYS (%)
Zn	8.7
Zn-0.15Mg	10.1
Zn-0.5Mg	14.2
Zn-1Mg	19.7
Zn-3Mg	8.2
Zn-0.5Al	8.7
Zn-1Al	11.2
AZ31	45.3

HIGHLIGHTS

1. Novel Zn alloy tubes were produced as potential materials for stent applications.
2. Properties were improved by optimizing compositional features and warm extrusion.
3. Al had a smaller effect on mechanical strength than Mg in Zn-based binary alloys.
4. Zn-0.5Mg showed the best combination of mechanical and corrosion performances.
5. EBSD study showed neither grain growth nor texture change near the laser cut edge.